Review

Oxide Cathodes: Functions, Instabilities, Self Healing, and Degradation Mitigations
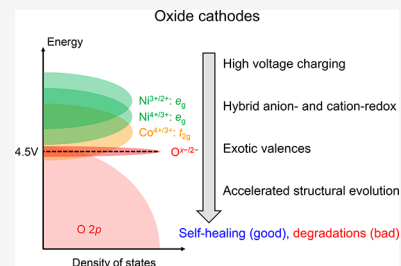
Yanhao Dong* and Ju Li*

ACCESS | Metrics & More | Article Recommendations | SI Supporting Information

ABSTRACT: Recent progress in high-energy-density oxide cathodes for lithium-ion batteries has pushed the limits of lithium usage and accessible redox couples. It often invokes hybrid anion- and cation-redox (HACR), with exotic valence states such as oxidized oxygen ions under high voltages. Electrochemical cycling under such extreme conditions over an extended period can trigger various forms of chemical, electrochemical, mechanical, and microstructural degradations, which shorten the battery life and cause safety issues. Mitigation strategies require an in-depth understanding of the underlying mechanisms. Here we offer a systematic overview of the functions, instabilities, and peculiar materials behaviors of the oxide cathodes. We note unusual anion and cation mobilities caused by high-voltage charging and exotic valences. It explains the extensive lattice reconstructions at room temperature in both good (plasticity and self-healing) and bad (phase change, corrosion, and damage) senses, with intriguing electrochemomechanical coupling. The insights are critical to the understanding of the unusual self-healing phenomena in ceramics (e.g., grain boundary sliding and lattice microcrack healing) and to novel cathode designs and degradation mitigations (e.g., suppressing stress-corrosion cracking and constructing reactively wetted cathode coating). Such mixed ionic-electronic conducting, electrochemically active oxides can be thought of as almost "metalized" if at voltages far from the open-circuit voltage, thus differing significantly from the highly insulating ionic materials in electronic transport and mechanical behaviors. These characteristics should be better understood and exploited for high-performance energy storage, electrocatalysis, and other emerging applications.

CONTENTS

1. INTRODUCTION

Oxide cathodes are key components in lithium-ion batteries (LIBs). Historically, intercalation cathodes were first demonstrated in TiS$_2$‖Li metal cell in 1976, where TiS$_2$ cathode, initially free of Li, was synthesized in the charged (fully delithiated) state and electrochemical lithiation was conducted during the first battery discharge half-cycle.[1,2] Similar examples include MoS$_2$ and NiPS$_3$ sulfides, V$_2$O$_5$ and MoO$_3$ oxides, and FeOCl oxyhalide.[3] Because the cell voltage is the highest when cathodes are fully delithiated (Li$^+$ and e$^-$ removal lowers the Fermi level and increases the voltage), the accessible upper redox potential is thus limited by the oxidation state of transition metal (TM) ions during synthesis under certain atmosphere (e.g., air, oxygen, inert, and reducing atmospheres), which is not expected to be significantly higher than the open-circuit voltage (OCV) of Li−air battery (∼2.91 V vs Li$^+$/Li). Therefore, the historical shift to initially Li-containing LiCoO$_2$ cathode not only increases the average redox potential, energy density, and anodic stability by switching the anion from easy-to-oxidize S^{2-} in sulfides (Pauling electronegativity χ = 2.58 for S) to more electronegative O^{2-} (χ = 3.44 for O) in oxides but also allows cathodes to be first charged/delithiated so that a high cell voltage (no longer constrained by the atmospheric synthesis conditions) up to 5 V (vs Li$^+$/Li) can in principle be achieved electrochemically.[2,4] Further, these Li-containing cathodes

make Li-free anodes such as graphite possible, which are safer than Li metal and historically critical to the success of LIBs.

Continuous developments in oxide cathodes lead to other chemistries, including layered $LiNi_{1-x-y}Co_xMn_yO_2$ (NCM) and $LiNi_{1-x-y}Co_xAl_yO_2$ (NCA),[5−8] layered Li-/Mn-rich cathodes (e.g., $xLi_2MnO_3\cdot(1-x)LiNi_{1/3}Co_{1/3}Mn_{1/3}O_2$, LRNCM),[9−11] spinel $LiMn_2O_4$ and $LiNi_{0.5}Mn_{1.5}O_2$,[12−15] polyanion cathodes (e.g., $LiFePO_4$),[16−18] and Li-excess cation-disordered rocksalt cathodes.[19,20] Elevating the upper cutoff voltage of these cathodes and achieving their full delithiation capacities would maximize the discharge capacity and energy density, yet this practice often results in accelerated capacity/voltage decay and shortened cycle life of the cathode and the full cell, caused by, for example, side reactions with and "pollution" of the electrolyte. Various forms of degradations have been identified, including impedance growth, irreversible surface and bulk phase trans-formations, intergranular/intragranular cracking of cathode particles, side reactions with the liquid organic electrolytes (the consumption can dry out the electrolyte), overgrowth of cathode−electrolyte interphases (CEIs), gassing (e.g., O_2 and CO_2), and TM dissolutions (which can migrate to and precipitate on the anode side, thus affecting the stability of solid electrolyte interphases, SEIs). Here we provide our perspectives to understand the functions, instabilities, damage buffering, and degradation mitigations of high-energy density oxide cathodes, with a special focus on layered cathodes ($LiCoO_2$, NCM, NCA, and LRNCM) that are of great scientific and technological interests. They also serve as good model systems to understand electrochemically active oxides. This review is organized in the following manner. Section 2 provides the basic knowledge on the atomic structure and lithium transport kinetics that enable proper functioning of the oxide cathodes and discusses the situations when the kinetics becomes sluggish and causes impedance issues. Section 3 applies electronic structure insight and local structure analysis to cathode design and explains the emergence of reversible oxygen redox activity in LRNCM. The unique electrochemical characteristics of LRNCM are discussed. Section 4 systemati-cally reviews the cathode degradation mechanisms and high-lights the strongly coupled electrochemomechanics, especially recently proposed stress corrosion cracking (SCC) of oxide cathodes immersed in liquid electrolytes. The unique degrada-tion modes of extensive lattice cavitation and layered-to-spinel bulk phase transformation for oxygen redox-active LRNCM are pointed out, and the underlying mechanism, bulk oxygen redox enhanced lattice oxygen mobility, shall be discussed and explained in section 5. While these cathodes suffer from various forms of degradation upon electrochemical cycling, section 6 discusses the peculiar mechanical properties, damage tolerance, and self-healing phenomena of certain electrochemically active oxides, which are unexpected for ceramics. Section 7 provides our perspectives on strategies to mitigate degradations, including the role of segregating dopants, microstructural design, reactive wetting enabled surface coating-plus-grain boundary infusion, Li concentration gradient produced by molten salt immunization, and novel electrolytes. Section 8 concludes and gives some forward-looking remarks.

2. ATOMIC STRUCTURE AND LITHIUM KINETICS

Oxide cathodes for LIBs are mixed ionic and electronic conductors with large "Li^0" storage and release capability. High Li^+ and electronic conductivities are preferred to minimize resistive loss. High capacity and voltage (for discharge) are preferred to maximize the energy density, and a robust anion-dominated host structure is preferred for cyclic Li^0 removal/insertion and safety. When a cathode is charged or discharged at a finite rate, a chemical-potential gradient is set along the radial direction of the cathode particles, which drives the fluxes of Li^+ and electrons with 1:1 ratio, thus effectively a Li^0 flux. According to the ambipolar diffusion theory (assuming local charge neutrality), the effective diffusivity D_{Li} of Li^0 can be expressed by the diffusivity D_{Li^+} of Li^+ and the diffusivity D_e of electronic species

$$D_{Li} = 2D_{Li^+}D_e/(D_{Li^+} + D_e) \tag{1}$$

For oxide cathodes, depending on the chemistry and state of charge, the electronic charge carriers can be small polaron or iterant electron, which even in the former case can have a much smaller migration barrier and thus much higher mobility than Li^+ (~12 700 times heavier than an electron). In the limit of $D_e \gg D_{Li^+}$, $D_{Li} \approx 2D_{Li^+}$, and it is Li^+ that rate limits the diffusion kinetics within each cathode particle.

For layered cathodes $LiMO_2$ with 1:1 Li-to-non-Li-metal ratio such as $LiCoO_2$, NCM, and NCA (M = Co, Ni, Mn, and Al; these are typically TM elements, except for Al used in NCA with ≤5% Al/M ratio, which otherwise makes NCA insulating and degrades electrochemical performance), oxygen anions are close-packed to form the structural framework, while Li and M both fill in octahedral sites, as is the case for the parent rocksalt structure. Because of distinct valence, cation radius, and hybridization between Li and M, there is a strong tendency for cation ordering in the system, forming alternating Li and TM layers within an O3 structure with −ABCABC− stacking sequence for the close-packed oxygen layers. The thickness of the TM layer is much smaller than that of the Li layer, because of stronger M−O bonds with shorter bond length than Li−O bonds. In a perfect layered structure, the Li layer can be viewed as an infinitely large two-dimensional (2D) plane for Li^+ diffusion via a Li vacancy mechanism, which offers facile kinetics in the accessible compositional range $Li_{1-x}MO_2$ ($0 < x < 1$) during electrochemical service. Here, Li^+ is designed to be ideally the only mobile ionic species, while TM and oxygen ions are ideally immobile within the structural framework, thus offering a reversible process of electrochemical charge and discharge. The Li^+ diffusion kinetics also depends on the Li slab size, as a larger slab size increases the size of the tetrahedral site (an intermediate site for Li^+ hopping between two octahedral sites) and the length between a hopping Li^+ and its neighboring transition-metal cation (thus lowering electrostatic energy penalty for Li^+ hopping). Such a correlation has been used to further increase Li^+ diffusion kinetics, especially for high-rate applications.[21−23]

However, Li^+ diffusion becomes problematic (i) when x approaches 0 in the fully lithiated state where the Li layer is fully occupied and Li vacancy concentration is low ("traffic jam"), and (ii) when degradations occur to transform the layered structure to some other phases close to pure TM oxides (such as rock-salt structured NiO and spinel structured Co_3O_4) that blocks percolative Li^+ diffusion pathway. For (i), it is most pronounced at the end of the discharge (cathodic) half-cycle, where the surface of the oxide particle equilibrates with the lower cutoff voltage (e.g., 3.0 V vs Li^+/Li for $LiCoO_2$, NCM, and NCA) and returns to the pristine $LiMO_2$ stoichiometry. It not only slows down Li^+ diffusion at the surface but also cuts off the longer-range Li^+ diffusion to lithiate the interior of the cathode particle (in the discharge half-cycle, the surface of the cathode

particles has a lower voltage and higher lithium concentration than the interior to maintain the inward Li^0 flux). Such sluggish Li^+ diffusion kinetics results in a large overpotential and rapid voltage drop at the end of the discharge half-cycle. As a result, D_{Li} measured by galvanostatic intermittent titration technique (GITT) shows 3−4 orders of magnitude decrease (Figure 1) as
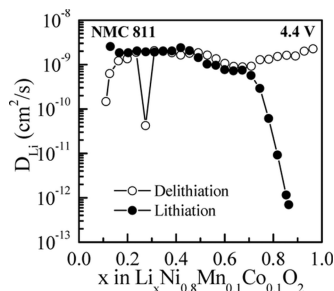

Figure 1. Dependence of D_{Li} (measured by GITT) as a function of lithiation amount x in $Li_xNi_{0.8}Mn_{0.1}Co_{0.1}O_2$ during delithiation (charge) and lithiation (discharge). Reproduced with permission from ref 24. Copyright 2019 American Chemical Society.

the discharge voltage approaches ∼3.0 V (vs Li^+/Li), even though the average bulk composition does not yet fully recover the original $LiMO_2$ stoichiometry[24] due to "traffic jam" at the surface. It results in asymmetric kinetics during charge (faster) and discharge (slower) because resolving the traffic jam at the surface by releasing Li^0 is easier than further inserting Li^0 into an already-jammed near-surface region, and thus, the layered cathodes appear to have lower discharge capacity than charge capacity in the first cycle, for the same discharge rate with the charge rate. For a good layered cathode material, the first-cycle Coulombic efficiency (CE) is typically around 90%. Such 10% first-cycle capacity loss for layered cathodes is mostly due to the asymmetric kinetics, as an elevated-temperature long-time constant-voltage hold at the lower cutoff voltage after the galvanostatic discharge step would recover most of the charge capacity.[24,25] Other factors affecting the initial irreversible capacity include the formation of CEIs, gassing, TM dissolution, and the formation of cation-densified phases at the oxide surface. As shall be discussed below, the formed CEIs and cation-densified surface phases would further slow down the lithiation kinetics during discharge. This contrasts with the SEI-

formation-dominated first-cycle capacity loss (consumption of the lithium reserve) for anodes such as graphite.

For (ii), because heavily delithiated cathodes containing an extreme level of lithium vacancies may not be thermodynamically stable, cathode decomposition tends to happen to eliminate these vacancies if the kinetics is allowed, such as at the surface of the cathode particles. (Bulk decomposition is possible upon heating,[26,27] including during the thermal runaway event in battery accidents.) This process involves oxygen loss, TM ion migration from TM layer to Li layer, TM reduction, and the formation of Li vacancy-free/lean, TM-enriched oxides with poor ionic and electronic conductivities. It is also called "TM condensation" as TM content gets enriched close to that in pure TM oxide[28] or cation densification as excess Li vacancies are removed.[29] For example, it can be expressed as

$$Li_{1-x}\square_xNiO_2 = (2 - x)Li_{(1-x)/(2-x)}Ni_{1/(2-x)}O$$
$$+ x/2O_2(gas) \qquad (2)$$
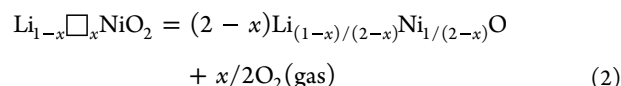
for the near-surface region of delithiated $LiNiO_2$. Here, $\square$ denotes Li vacancy created during electrochemical delithiation, and $0 < x < 1$. Obviously, the decomposition reaction would be more severe with larger x, i.e., at higher charge voltages, and the product $Li_{(1-x)/(2-x)}Ni_{1/(2-x)}O$ has TM content close to that of NiO. With x close to 1 at the surface, it eventually leads to the formation of rocksalt NiO (insulating to both electron and Li^+) following

$$Li_0\square_1NiO_2 = NiO + 1/2O_2(gas) \qquad (3)$$
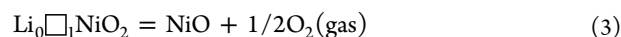
A thick NiO-like phase has been widely observed at the surface of degraded Ni-rich layered cathodes[30−33] (Figure 2a), which is resistive and causes impedance growth and capacity decay. In such a NiO-like phase, (Li,M) cations fill the octahedral sites quasi-randomly so that the cubic symmetry of the rocksalt parent structure is partially recovered; Ni has mixed +2 (major) and +3 (minor) valence with poor electronic conductivity (NiO is known to be an electronic insulator with strong correlation of Ni 3d electrons, which was used to propose the model of Mott insulator[34]); Li concentration is depleted to exclude percolating Li^+ diffusion pathway so that it is no longer electrochemically active. These are the typical features for Li-poor (TM-rich) cation-disordered rocksalt structure TM oxides, which are different from the electrochemically active Li-rich (TM-poor) cation-disordered rocksalt structure TM oxide cathodes.[19,20]
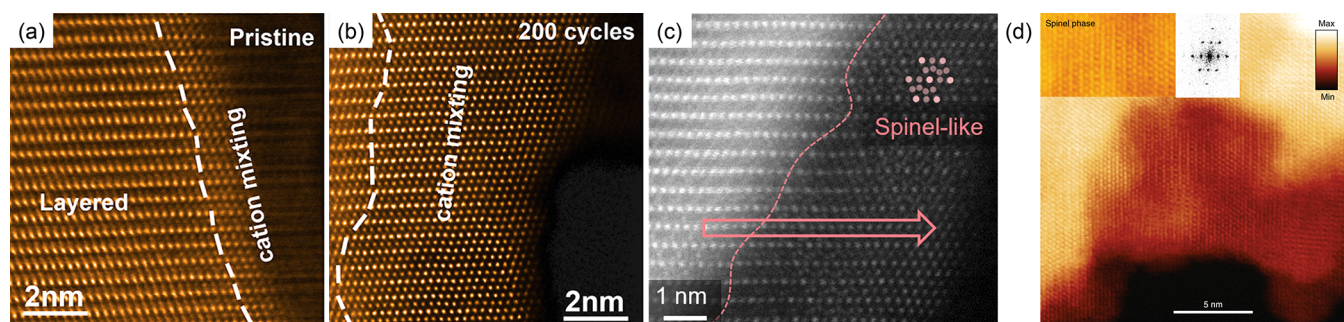

Figure 2. (a) A thin layer of NiO-like disordered-rocksalt phase at the surface of pristine $LiNi_{0.76}Mn_{0.14}Co_{0.10}O_2$ before electrochemical cycling. (b) A thick layer of NiO-like disordered-rocksalt phase at the surface of $LiNi_{0.76}Mn_{0.14}Co_{0.10}O_2$ after 200 cycles at 0.33 C between 2.7 and 4.3 V (vs Li^+/Li) at room temperature. Reproduced with permission from ref 30. Copyright 2020 American Chemical Society. (c) Formation of Co_3O_4-like spinel phase at the surface of $LiCoO_2$ after 100 cycles at 1 C between 3.0 and 4.45 V (vs Li^+/Li) at 25 °C. Reproduced with permission from ref 39. Copyright 2019 Wiley-VCH. (d) Formation of spinel phase at the surface of cycled $Li_{1.2}Mn_{0.55}Ni_{0.15}Co_{0.1}O_2$. Reproduced with permission from ref 46. Copyright 2018 The Author(s).

For Ni-rich layered cathodes, the NiO-like cation-disordered rocksalt surface phase forms not only in electrochemical degradation but also during synthesis.[35,36] Meanwhile, partial Li/Ni cation mixing (antisite defect, typically with a few percent fraction when normalized by the amount of Li, or M, thus still having Li and TM contents close to those of LiMO_2, respectively) also takes place in the bulk, which is often characterized by Rietveld refinement of the powder X-ray diffraction (XRD) data. The formations of both NiO-like surface phase and cation-mixed bulk phase are more pronounced in a less oxidizing atmosphere and at higher temperatures, which favors oxygen loss and partial reduction of Ni^{3+} to Ni^{2+}. Compared to Ni^{3+}, Ni^{2+} has a charge and a size closer to Li^+ (Shannon radius for 6-fold coordination is 0.69 Å for Ni^{2+}, 0.56/0.6 Å for low-/high-spin Ni^{3+}, and 0.76 Å for Li^+) and smaller octahedral-site crystal-field stabilization energy ($-0.85\Delta_o$ for Ni^{2+} and $-1.27\Delta_o$ for Ni^{3+}). (Following ref 37, we use Δ_o to denote octahedral-site energy splitting, assume tetrahedral-site energy splitting $\Delta_t = 0.44\Delta_o$, and ignore electron pairing energy. Electronic configurations are taken as $t_{2g}^6 e_g^2$ for octahedral Ni^{2+}, $e_g^4 t_{2g}^4$ for tetrahedral Ni^{2+}, $t_{2g}^6 e_g^1$ for octahedral Ni^{3+}, and $e_g^4 t_{2g}^3$ for tetrahedral Ni^{3+}.) Therefore, there is less tendency for Ni^{2+} to be cation-ordered. Ni^{2+}, once formed, tends to migrate to Li layer and substitute octahedral-site Li^+.

A moderate amount of Li/Ni cation mixing (e.g., less than 2−3%) is beneficial to the cycling stability due to the pillar effect,[38−40] where Ni^{2+} at Li site suppresses TM slab sliding induced bulk phase transformations at high voltages. However, as the levels of bulk cation mixing and the formation of NiO-like surface phase both depend on the synthesis conditions (especially the precursors, gas atmosphere and temperature) and are correlated with each other, more severe bulk cation mixing often indicates the formation of a much thicker NiO-like surface phase (surface is easier to lose oxygen and to be reduced). As the former can be easily characterized by XRD whereas the latter requires high-resolution microscopy, cation mixing is widely used to describe the "quality" of Ni-rich layered cathodes, and 5% or more cation mixing often results in poor electrochemical performance. One may argue that increasing bulk cation mixing from 2% to 3% to 5% cannot impose a severe diffusion bottleneck in the lattice, but the concurrent thickening of the NiO-like surface phase can severely increase the impedance. As high temperature and low PO_2 promote NiO-like surface phase, for synthesizing Ni-rich layered cathodes with ≥60% Ni/M, the solid-state lithiation step is often conducted in flowing oxygen (instead of air for LiNi$_{1/3}$Co$_{1/3}$Mn$_{1/3}$O$_2$ and LiNi$_{0.5}$Co$_{0.2}$Mn$_{0.3}$O$_2$) and at ≤800 °C (e.g., lower temperatures of 700 °C was used for LiNiO$_2$ and 750 °C for LiNi$_{0.9}$Co$_{0.05}$Mn$_{0.05}$O$_2$).[41,42] Such low lithiation temperature requires high-reactivity precursors with uniform TM distribution, which has not yet been made by "all-solid-state" synthesis method and is currently obtained by a wet-chemistry coprecipitation method. Hydroxide/carbonate precursors Ni$_{1−x−y}$Co$_x$Mn$_y$(OH)$_2$/Ni$_{1−x−y}$Co$_x$Mn$_y$CO$_3$ coprecipitated from aqueous solutions of TM sulfates (e.g., NiSO$_4$, CoSO$_4$, and MnSO$_4$) are commercially available and become the preferred routes to synthesizing Ni-rich layered cathodes NCM, NCA (NCA does not contain Mn or Al in the hydroxide/carbonate precursors, and Al is added by mixing the precursors with Al^{3+} source before final high-temperature lithiation step; Al^{3+} cannot be uniformly coprecipitated with Ni^{2+} and Co^{2+} due to very different precipitating pH) as well as Li-/Mn-rich layered cathodes. Upon heating, these precursors

would decompose into fine oxide particles at ~500 °C and react with mixed lithium salts, followed by cation ordering and phase formation at higher temperatures. The microstructure of the final cathode product strongly depends on the morphology of the precursors, which can be effectively tuned by synthesis conditions of the coprecipitation technique. The microstructure of the resulting secondary particle (effectively a polycrystal of primary particles/grains, with some porosity) would have a substantial effect on the electrochemical performance.

Back to the side reaction product from cation densification in (ii), instead of rocksalt surface phase for Ni-rich layered cathodes, spinel surface phases have been frequently reported for degraded LiCoO$_2$[39,43−45] (Figure 2b) and Li-/Mn-rich layered cathodes[46−49] (Figure 2c). Note these TM-rich spinel surface phases are Co$_3$O$_4$- and Mn$_3$O$_4$-like, where Co^{2+} and Mn^{2+} occupy the tetrahedral site, and they are resistive to Li$^+$ diffusion and harmful to electrochemical performance, thus considered "bad" spinels. They should not be confused with LiMn$_2$O$_4$-like spinel ("good" spinel), where Li$^+$ occupies the tetrahedral site and allows fast three-dimensional Li$^+$ diffusion. For cation densified products, the preference of spinel structure for Co- and Mn-rich compositions (average TM valence 8/3 = 2.67, with Co^{2+} and Mn^{2+} at tetrahedral site) vs rocksalt structure for Ni-rich ones (average TM valence 2, with Ni^{2+} at octahedral site) is interesting, which cannot be explained by the charge or size effect. Cations with higher valence and larger radius would prefer octahedral over tetrahedral sites because the former provides more effective screening and has a larger volume. Shannon radius for 6-fold coordination is 0.69 Å for Ni^{2+}, 0.65 Å for low-spin Co^{2+}, and 0.67 Å for low-spin Mn^{2+}; for 4-fold coordination, it is 0.55 Å for Ni^{2+}, 0.58 Å for Co^{2+}, and 0.66 Å for Mn^{2+}. Because Ni^{2+} is the smallest among the three, the charge and size argument would predict more tetrahedral site preference of Ni^{2+} compared to Co^{2+} and Mn^{2+}, which is opposite to the experimental observations. The estimation from the octahedral-site crystal-field stabilization energy does not explain either, as it gives $-0.85\Delta_o$ for Ni^{2+}, $-1.27\Delta_o$ for Co^{2+}, and $-2.0\Delta_o$ for Mn^{2+}, which again gives prediction against experimental observations. (Here the electronic configurations are taken as $t_{2g}^6 e_g^2$ for octahedral Ni^{2+}, $e_g^4 t_{2g}^4$ for tetrahedral Ni^{2+}, $t_{2g}^6 e_g^1$ for octahedral Co^{2+}, $e_g^4 t_{2g}^3$ for tetrahedral Co^{2+}, $t_{2g}^5 e_g^0$ for octahedral low-spin Mn^{2+}, and $e_g^2 t_{2g}^3$ for tetrahedral high-spin Mn^{2+}; octahedral high-spin Mn^{2+} has zero octahedral-site crystal-field stabilization energy.) Instead, we propose that it is due to the TM redox energies of Ni^{2+}/Ni^{3+}, Co^{2+}/Co^{3+}, and Mn^{2+}/Mn^{3+} redox couples in pure TM oxides. When annealed in air, for nickel oxides, NiO (rocksalt) is the stable form, suggesting that air is not oxidizing enough to oxidize Ni^{2+} to Ni^{3+} and a high equilibrium oxygen partial pressure lnPO_2^{eq}(Ni^{3+}/Ni^{2+}) for Ni^{3+}/Ni^{2+} redox couple. For cobalt oxides annealed in air, Co$_3$O$_4$ (spinel) is stable at low temperatures (<900 °C) and CoO (rocksalt) is stable at high temperatures (>900 °C), suggesting an intermediate lnPO_2^{eq}(Co^{3+}/Co^{2+}) for Co^{3+}/Co^{2+} redox couple. For manganese oxides annealed in air, Mn$_3$O$_4$ (spinel) readily forms at high temperatures (>1000 °C), suggesting a lower lnPO_2^{eq}(Mn^{3+}/Mn^{2+}) for Mn^{3+}/Mn^{2+} redox couple. Therefore, lnPO_2^{eq}(Ni^{3+}/Ni^{2+}) > lnPO_2^{eq}(Co^{3+}/Co^{2+}) > lnPO_2^{eq}(Mn^{3+}/Mn^{2+}) in pure TM oxides, which indicates that electronic energy level follows the rank of Ni^{3+}/Ni^{2+} < Co^{3+}/Co^{2+} < Mn^{3+}/Mn^{2+}. It also suggests that for cation-densified surface phase that has gone through oxygen loss and TM reduction, it is more difficult to retain Ni^{3+} than Co^{3+} and Mn^{3+} in the solid phase, and it is the
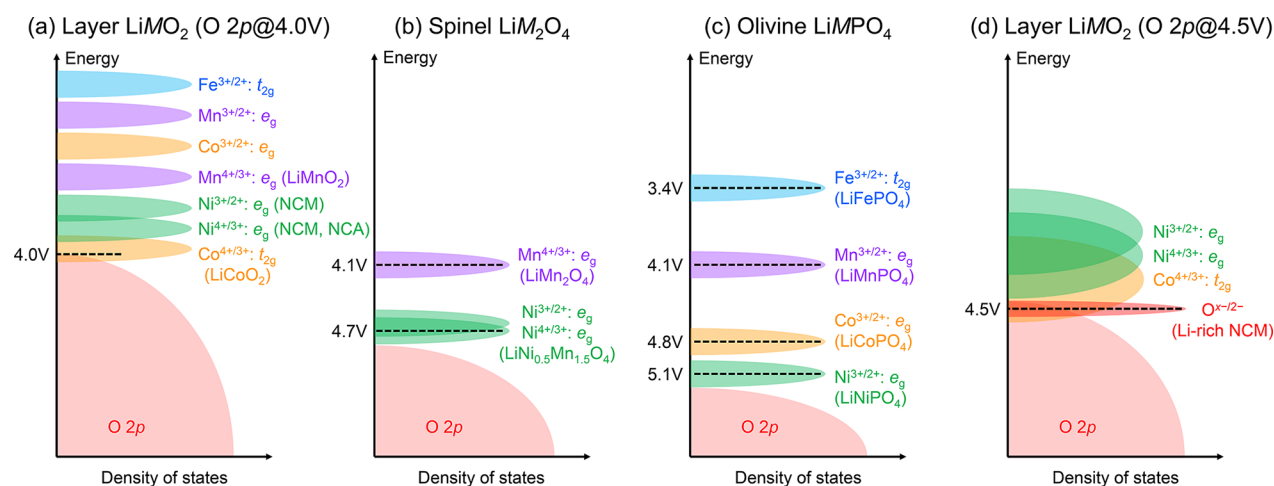
Figure 3. Schematic diagram comparing the energy levels of different redox couples and DOS of (a) layered cathode $LiMO_2$ assuming the top of O $2p$ band pinned at 4.0 V (vs Li$^+$/Li), (b) spinel cathode LiM_2O_4, (c) olivine cathode $LiMPO_4$, and (d) modified (a) assuming the top of O $2p$ band pinned at 4.5 V (vs Li$^+$/Li). The energy dispersion along the y axis is for the guidance of the eyes.

electronic energy level that determines the average TM valence (+2 for rocksalt and +8/3 for spinel), the TM-to-O stoichiometry, and the phase of the surface side-reaction products.

3. ELECTRONIC STRUCTURE PERSPECTIVE

Electronic energy level plays a central role in the function and stability of oxide cathodes. Utilizing the voltage profile of the discharge curve at a low rate and assuming a rigid band structure that does not evolve at different states of charge, the approach of constructing schematic diagram comparing the energy levels of different redox couples and density of states (DOS) is a useful method for cathode design and optimizations. This was well recognized by Goodenough since the initial introduction of high-voltage oxide cathodes,[2,4,50,51] whose anodic charging voltage stability window was presumed to be set by the top of O $2p$ band that lies at a much lower electronic energy than the top of S $2p$ band. In LiCoO$_2$, the top of O $2p$ band was estimated to be at ~4.0 V (vs Li$^+$/Li) and there is an overlap between Co$^{4+/3+}$ redox couple and O $2p$ band.[50,51] Upon removal of over ~0.55 Li per LiCoO$_2$, there is a crossover from TM redox to oxygen redox, with itinerant holes with strong O $2p$ band characteristics. This could potentially cause oxygen instability (i.e., chemical instability of oxygen ions) in the cathode material, such as the formation of peroxide group and oxygen gas evolution. However, the early estimation of 4.0 V vs Li$^+$/Li is probably too low, as nowadays, high-voltage LiCoO$_2$ is readily available and can be stably cycled up to 4.6 V (vs Li$^+$/Li), with a first-cycle charge capacity of >230 mAh/g or 0.84 Li removal per LiCoO$_2$.[52−54] It indicates that while the thermodynamic anodic stability window is set by the chemistry and crystal structure, the oxygen instability can be kinetically suppressed in real batteries. This is especially true for oxygen gas evolution reaction (OER) that typically has a larger overpotential (than, for example, hydrogen evolution reaction), and oxide stabilization strategies such as lattice doping, surface coating, and modifications of the organic liquid electrolytes have been synergistically utilized to enable high-voltage LiCoO$_2$ with extended cycle life. These in turn encourage the development of HACR cathodes with high capacities and energy densities.

Within the same layered structure framework, the relative positions of other TM redox couples can be determined and plotted schematically (Figure 3a) according to the following experimental observations. In NCM electrochemical cycling, the lowest TM valence is +2 for Ni, +3 for Co, and +4 for Mn, which indicates a higher electronic energy level (i.e., lower redox voltage) of Mn$^{4+/3+}$ than Ni$^{3+/2+}$. Under the same charging cutoff voltage, NCM with initially mixed Ni^{2+} and Ni^{3+} and NCA with initial Ni^{3+} have higher charging capacity than LiCoO$_2$ with initial Co^{3+}, which indicates a higher electronic energy level of Ni$^{4+/3+}$ than Co$^{4+/3+}$. Therefore, the electronic energy level follows the rank of Mn$^{4+/3+}$ > Ni$^{3+/2+}$ > Ni$^{4+/3+}$ > Co$^{4+/3+}$. These are the most useful TM redox couples in layered cathodes, as is the case for LiMnO$_2$, NCM, NCA, and LiCoO$_2$. Among them, LiMnO$_2$ is not as widely used as the latter two because of structural instability.[37,55] With a small octahedral-site crystal-field stabilization energy (−0.42Δ$_o$ for Mn^{3+}, electronic configuration taken as $t_{2g}^3 e_g^1$ for octahedral high-spin Mn^{3+} and $e_g^2 t_{2g}^2$ for tetrahedral high-spin Mn^{3+}), Mn would easily migrate from octahedral to tetrahedral sites that transforms the layered structure into a bad spinel. The strong Jahn−Teller effect for Mn^{3+} also causes distortion in the lattice and degrades the material upon cycling. Other TM redox couples such as Co$^{3+/2+}$, Mn$^{3+/2+}$, and Fe$^{3+/2+}$ lie at higher electronic energies and thus are less useful in cathodes, and +2 valence TM ions cannot be readily put into the layered $LiMO_2$ that requires an average initial valence of +3 for M.

Mn is more earth-abundant and much cheaper than Ni and Co. The rule-of-thumb so far is that in order to better utilize the Mn$^{4+/3+}$ redox couple without causing structural instability, the average Mn valence should be higher than +3 throughout the cycling. Good cycling stability has been achieved in spinel LiMn$_2$O$_4$ with average Mn valence of +3.5 in the discharged state and approaching +4 in the fully charged state. The 0.5 Li removal per TM obviously lowers the capacity of spinel cathodes compared to 1 Li per TM in layered cathodes, yet the energy density is partially recovered due to lowered electronic energy of TM redox in the spinel structural framework relative to the layered structure (Figure 3b). For example, Mn$^{4+/3+}$ redox couple lies at ~4.1 V (vs Li$^+$/Li) in LiMn$_2$O$_4$ and Ni$^{3+/2+}$ and Ni$^{4+/3+}$ redox couples lie at ~4.7 V (vs Li$^+$/Li) in LiNi$_{0.5}$Mn$_{1.5}$O$_4$, all of which are higher than the corresponding ones in the layered structure.[13,14,50,56] Here, also note that the voltage curves of LiMn$_2$O$_4$ and LiNi$_{0.5}$Mn$_{1.5}$O$_4$ show obvious
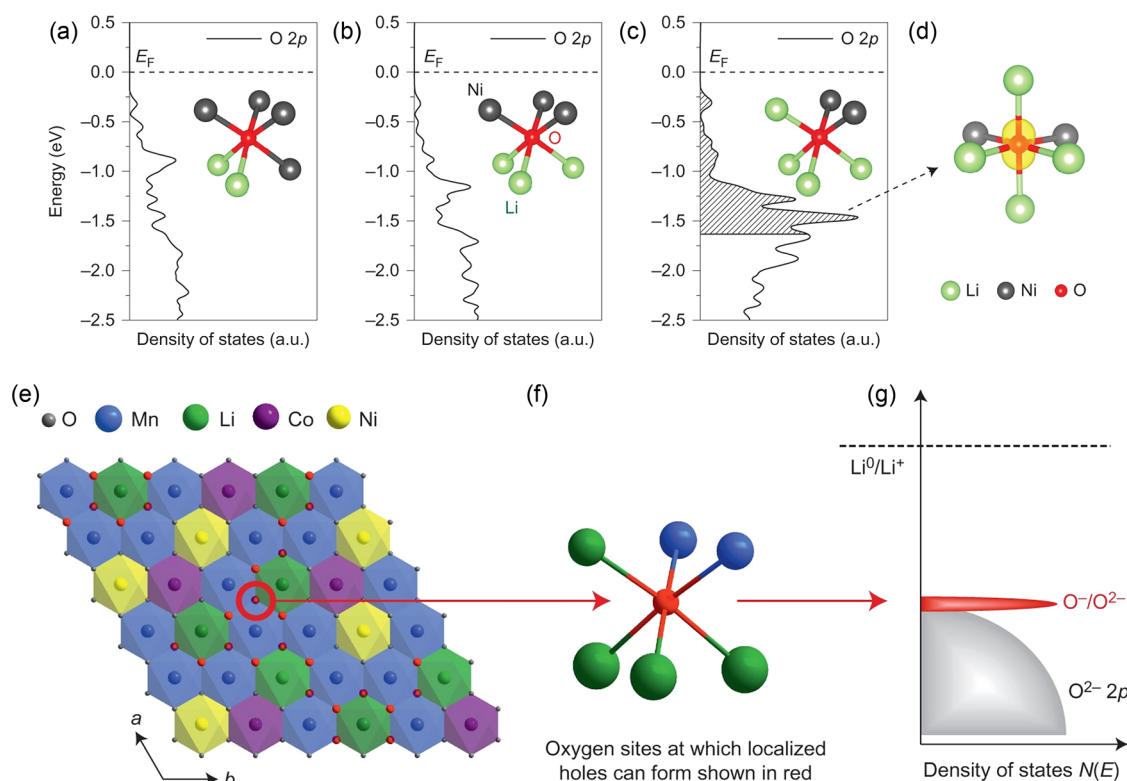
Figure 4. Calculated partial DOS of an oxygen coordinated by (a) two Li and four Ni, (b) three Li and three Ni, and (c) four Li and two Ni in a cation disordered LiNiO$_2$. The decreased O−Ni coordination number from (a) to (c) increases the high-energy DOS close to the Fermi level E_F as shown by (d) the isosurface of the charge density between −1.64 and 0 eV (vs E_F) of the oxygen in (c). Reproduced with permission from ref 71. Copyright 2016 Nature. (e) Honeycomb-type cation ordering in TM layer of LRNCM creates (d) oxygen coordinated by four Li and two Mn and (f) nonbonding orbital of O 2p states at the top of the broad O 2p band. Reproduced with permission from ref 72. Copyright 2016 Nature.

voltage plateaus, indicating a narrow redox DOS in the electronic energy axis. In comparison, the voltage curves of NCM, NCA, and LiCoO$_2$ are more slopy, indicating more distributed redox DOS. This is likely due to the stronger sensitivity to the microscopic Li$^+$ distribution (the Li−Li coverage effect, which is stronger in layered compounds due to shorter Li−Li distance).

The energy of a TM redox couple depends on the element, its valence, the covalent component (hybridization) of its bonding with the nearest neighbors (i.e., the local structure around a TM ion), and the ionic component (Madelung energy) of its bonding with longer-range ions within the structural framework.[50] The lowered electronic energy of Mn$^{4+/3+}$, Ni$^{3+/2+}$, and Ni$^{4+/3+}$ redox couples in spinel is primarily due to changes in the Madelung energy, which is often termed the inductive effect. For Li$_{1-x}$Mn$_2$O$_4$, Li$^+$ ordering at tetrahedral site already causes ∼0.15 V shift in the voltage of Mn$^{4+/3+}$ redox couple when cycled between $x = 0$ and 1, and Li$^+$ position change from tetrahedral to octahedral site causes >1 V shift when cycled between $x = -1$ and 0 (i.e., overdischarge of LiMn$_2$O$_4$). The inductive effect is even stronger in polyanion cathodes, such as olivine LiMPO$_4$, where Fe$^{3+/2+}$ redox couple lies at ∼3.4 V, Mn$^{3+/2+}$ at ∼4.1 V, Co$^{3+/2+}$ at ∼4.8 V, and Ni$^{3+/2+}$ at ∼5.1 V (Figure 3c).[16,57−60] These redox voltages are much higher than the corresponding ones in the layered structure, and it enables the use of the most abundant TM element, Fe, in LiFePO$_4$ with a huge commercial success. LiMnPO$_4$ and Li(Fe,Mn)PO$_4$ with higher voltages and energy densities are also under development for extended cycle life. The olivine cathodes generally have relatively poor ionic and electronic conductivities and undergo two-phase reactions in the

coarse particles that rate-limits their electrochemical performance. Therefore, they are typically coated with conductive carbon and produced in nanoparticle form that recovers a solid-solution reaction mechanism.[61−63] Nevertheless, there are still distinct plateaus in their voltage curves, again indicating narrowly dispersed redox DOS.

While the above understandings are mainly on TM redox for cathode functioning, better oxygen stability is also gained in spinel and olivine cathodes due to lowered electronic energy of O 2p band, based on the voltages of Ni$^{4+/3+}$ and Ni$^{3+/2+}$ redox couples that are assumed not to overlap with O 2p band. This is supported by the experimental observations that spinel and olivine cathodes have better thermal stability and thus safety than layered ones.[64−67] (In the thermal runaway event of battery accidents, charged cathodes often release oxygen gas and/or radicals, which serve as oxidant to the self-accelerating exothermal reactions with anode material and electrolyte.) The lowered O 2p band energy can be understood from strong Mn 3d−O 2p hybridization (especially for Mn^{4+}) and three-dimensionally connected MnO$_6$ octahedron network in spinel cathodes and strong covalent P−O bond in olivine cathodes, both of which are closely related to the nearest-neighbor bonding, i.e., local structure of O. The strong Mn^{4+}−O$^{2−}$ bond also contributes to the oxygen stability of NCM, where higher Mn contents are known to increase the thermal stability and safety.[67,68] To date, the superior oxygen stability of high-voltage (e.g., with redox voltage >4.6 V) spinel and olivine cathodes have not been fully utilized, primarily limited by other degradation mechanisms of the cathode and the full cell, especially the anodic stability of the electrolyte. Future

developments of advanced electrolytes in liquid, solid, or mixed form may make full use of such high-voltage TM redox couples, which compensates for the intrinsically lower capacity and ion-packing density (thus crystal density) of spinel and olivine cathodes compared to layered ones.[69,70]

Applying the local structure analysis of O to LRNCM, which is also a layered cathode but with Li^+ substitution and Li_2MnO_3-type Li/TM ordering in the TM layer, leads to the emergence of active, reversible oxygen anion-redox. Recall that the layered structure can be viewed as a cation-ordered rocksalt structure, and O is octahedrally coordinated with six cation nearest-neighbors. In $LiMO_2$, O is coordinated by three Li and three M (mainly TM elements) with $3 \times Li-O-M$ configurations, where $d-p$ hybridization lowers the energy of O $2p$ band. In contrast, in Li_2MnO_3, O is coordinated by four Li and two Mn with $2 \times Li-O-Mn$ configurations and $1\times$ axial $Li-O-Li$ configuration. Because there is minimal hybridization between Li and O, the nonbonding O $2p$ orbital in axial $Li-O-Li$ configuration constitutes oxygen redox state at the top of the broad O $2p$ band (Figure 4).[71−73] Apparently, this analysis also holds for LRNCM, which accounts for the long, flat voltage plateau at ~4.5 V (vs Li^+/Li, contributing to ~200 mAh/g capacity in $Li_{1.2}Mn_{0.48}Ni_{0.16}Co_{0.16}O_2$ when charged to 4.8 V) in the first charge half-cycle beyond the accessible TM redox couples ($Ni^{3+/2+}$, $Ni^{4+/3+}$, and $Co^{4+/3+}$, contributing to ~120 mAh/g capacity in $Li_{1.2}Mn_{0.48}Ni_{0.16}Co_{0.16}O_2$). Similar local structure analysis of O has been extended to interpret the oxygen redox activity in Li-excess cation-disordered rocksalt cathodes[74−76] and Li-rich spinel cathodes[77] as well as other functional oxides,[78] the oxygen instability at surface and interfaces, and the functioning of protective cathode coating.[79] The flatness of the voltage plateau is interesting to note, as no similar shapes have been identified for TM redox couples in layered cathodes, including NCM, NCA, $LiCoO_2$, and LRNCM. In fact, it represents an electrochemical demonstration for the "pinning" of a redox couple, i.e., further electron removal does not cause lowering in the electronic energy. The pinning is now clearly seen in LRNCM, by $Li-O-Li$ configuration and nonbonding orbital of O $2p$ states, which can be used to place the top of the O $2p$ band at 4.5 V (vs Li^+/Li). This allows us to replot Figure 3a as Figure 3d, still assuming an overlap between $Co^{4+/3+}$ redox couple and O $2p$ band. (In principle, the dispersion of a redox couple in the energy axis of the schematic should represent the degeneracy of the corresponding DOS and the area should be the same for one-electron redox couple. However, it is difficult to quantify and thus not accounted for simplicity. The energy dispersion in Figure 3 is only for the guidance of the eyes.)

The Li richness (e.g., 1.2 Li per $Li_{1.2}Mn_{0.48}Ni_{0.16}Co_{0.16}O_2$, equivalent to 1.5 Li per TM) and the HACR action provide LRNCM a high discharge capacity of 250−300 mAh/g when cycled between 2.0 and 4.8 V (vs Li^+/Li), compared to ~205/220 mAh/g for Ni-rich cathode cycled between 3.0 and 4.3/4.5 V (vs Li^+/Li), and ~220 mAh/g for high-voltage $LiCoO_2$ cycled between 3.0 and 4.6 V (vs Li^+/Li). While a larger upper cutoff voltage is required to activate the oxygen redox in the first charge half-cycle, a smaller lower cutoff voltage is also required for LRNCM due to the slow kinetics and the voltage hysteresis of the oxygen redox. Compared to other layered cathodes, LRNCM has the following distinct features in the electrochemical behaviors: (i) There is typically a huge change in the voltage curve between the first charge half-cycle and subsequent ones, as the 4.5 V voltage plateau during the first charge is no longer observed in subsequent cycles. This is often attributed to

the irreversible structural changes (e.g., TM migration and lattice reconstruction) when LRNCM is first charged/discharged. Interestingly, such a drastic structural change correlates with the activation of the anion redox reaction. In section 5, we shall explain that the oxygen mobility (which is the slowest moving species in the discharge state) also drastically increases when the anion redox is activated. One may argue that the hugely enhanced oxygen ion mobility further contributes to the drastic structural change, as all species (lithium ion, transition metal ion, and oxygen ion) become quite mobile, at least at the nanoscale. We suspect that the structural change is not only thermodynamically favorable but also kinetically accelerated by the activated oxygen redox and the altered TM-O bonding characteristics. (ii) The voltage efficiency and energy efficiency of LRNCM are relatively low. This is due to the hysteresis associated with the oxygen redox, which exists even under quasi-OCV conditions, e.g., after long-time relaxations in GITT measurements.[80,81] The OCV hysteresis indicates that the sluggish oxygen redox does not follow a linear response to the driving force as is the case in diffusion but requires an overpotential in analogy to a chemical reaction. (iii) Although with an upper cutoff voltage of 4.8 V (vs Li^+/Li), capacity decay of LRNCM can be relatively slow.[82,83] This is likely to be due to the catalytic inactivity of Mn^{4+}, which is the main cation at the surface of LRNCM, while Ni^{3+}, Ni^{4+}, Co^{3+}, and Co^{4+} in NCM, NCA, and $LiCoO_2$ are more oxidizing and catalytically more active (thus widely used in oxide catalysts for oxygen evolution reaction). (iv) There is a gradual decay in the average discharge voltage (i.e., voltage decay) associated with the shape change of the voltage curves upon cycling. This is a unique feature of LRNCM and causes decay in the discharge energy density. The voltage decay holds even at low rates and under quasi-OCV conditions: the lowered redox voltage indicates an evolving bulk structure of LRNCM. This differs from NCM, NCA, and $LiCoO_2$, whose degradations are mainly due to impedance (kinetics) and whose voltage profiles under OCV conditions remain largely the same before and after cycling.[39]

The unique electrochemical characteristics of LRNCM are closely related to oxygen redox. Extensive efforts have been made to resolve the underlying mechanism, especially on its relationship with voltage hysteresis and voltage decay that limit the practical applications of LRNCM.[80,81,83] The proposed mechanisms include the formation of peroxide- and superoxide-like oxygen dimers,[84−86] the oxidation of nonbonding O $2p$ orbitals with localized oxygen hole states,[71−73] the formation of π-bonded orbitals from hybridized TM and oxygen states,[87] and the formation of molecular O_2 trapped in the bulk.[88−90] The last proposal is supported by high-resolution resonant inelastic X-ray scattering (HR-RIXS) spectroscopy data,[88] and the resolved low-energy loss features reveal a progression of peaks from transitions to different vibrational energy levels, which agree well with the vibrational spectrum of molecular O_2. It is consistent with our interpretation that the OCV hysteresis indicates the requirement of a reaction overpotential for the sluggish oxygen redox, namely the breakage and reformation of the O−O covalent bond. A better and clearer understanding of the oxygen redox mechanism would help to develop LRNCM further, as well as other Li-rich, oxygen-redox-active oxide cathodes. It is also clear that TM cation migration plays a significant role as the anion migration in the time-dependent HACR voltage, so the coupled cation and anion mobilities (CCAM) is a frontier of research for understanding high-energy-density HACR cathodes.

4. COUPLED ELECTROCHEMOMECHANICAL DEGRADATIONS

Battery cathodes need to be cycled with an extended lifetime, and they suffer from coupled electrochemomechanical degradations[91] such as chemical corrosion, electrochemical side reactions, and mechanical cracking. The degradations affect the functioning of cathodes as well as other components in the battery ecosystem, such as the electrolyte and the anode. The cathodes interact with the environment chemically and electrochemically. When cathodes are charged to high voltages, the bulk materials are not thermodynamically stable, and upon heating, they would decompose, release oxygen gas, and undergo exothermic reactions.[92,93] This is intimately connected to battery safety, especially thermal runaways in battery accidents, and the intrinsic safety of a cathode is often evaluated by comparing the temperature and heat generation of the exothermic reactions in the differential scanning calorimetry (DSC) measurements of the charged cathodes. Under normal battery operation temperatures, the bulk decomposition is kinetically suppressed, and side reactions mostly take place at the cathode surface and with interactions with the electrolyte. Oxygen gas can evolve from the cathode surface as a gaseous component of the side reaction products.[92,93] Other gases such as CO_2 can also evolve due to the oxidization of the organic electrolytes, which either directly involves oxygen molecule/radicals generated from the oxidizing charged cathodes or comes from the anodic decomposition of the electrolytes catalyzed by the TM ions at the cathode surface.

The side reaction products in the solid form are complicated and can generally be classified into two regions. The first region is on the oxide side of the original cathode–electrolyte interface, i.e., the cation-densified surface phase as we discussed in section 2, such as the NiO-like rocksalt phase at the surface of degraded Ni-rich NCM and the Co_3O_4-like spinel phase at the surface of degraded $LiCoO_2$. The second region is on the electrolyte side of the original cathode–electrolyte interface and is termed as CEIs.[94−98] CEIs form because of chemical incompatibilities between the charged cathodes and the electrolyte. CEIs are heterogeneous multiphase composites with potentially both organic and inorganic constituents and the chemical compositions could also vary across the thickness. The cation-densified surface phase and CEIs are not bad by themselves, and their formation passivates the cathode surface to suppress the continuous side reactions. However, their overgrowths are bad and cause significant impedance growth and decay in capacity, energy density, and energy efficiency of the degraded cathodes.

The interesting bilayer character of the cathode passivation is overlooked in the literature. Recall that on the anode side, SEIs, which are also heterogeneous multiphase composites, form as the passivation layer.[99−102] While there are still unknowns for SEIs, the established theoretical picture states that a good SEI layer should be thin and stable upon cycling and it should be primarily a Li^+ conductor but an electronic insulator, so that the lithiation process takes place at the interface between SEIs and the anode. The blockage of electron transport to the electrolyte suppresses the cathodic reduction of the electrolyte and the side reactions between the lithiated anode and the electrolyte. Considering the similarities, the insight has been extended to CEIs to make them Li^+-conductive and electron-insulating. Experimentally, CEIs with less carbon-rich organic components and more fluorine-rich inorganic (LiF- and PO_xF_y-like) components have been reported to stabilize the cathode–

electrolyte interface at high charge voltages.[103] Here, the CEI layer blocks electron transport to suppress the anodic oxidation of the electrolyte and physically separates the oxide surface from the electrolyte to minimize the catalytic effect of the former. For the role and design rules of the oxide surface phase, the same guidance, high Li^+ conductivity and low electronic conductivity, are often quoted, including in constructing protective cathode coatings as the artificial surface phase. While Li^+ solid electrolyte-like coatings (e.g., lithium phosphorus oxynitride, LiPON)[104] have been reported to improve the cathode cyclability, nanoscale coatings made of ionic and electronic insulators (at least for their bulk form, e.g., Al_2O_3 and AlF_3),[105,106] mixed ionic and electronic conductors (e.g., $LiNi_{0.5}Mn_{1.5}O_4$),[107] and metallic glass (e.g., CoB_x)[79] have also shown their effectiveness. Therefore, we propose that the optimal cation-densified surface phase or the artificial cathode coating should not block the electron transport. Indeed the proper functioning of cathodes requires ambipolar transport of Li^0, thus electrons, for each particle, and the task of electron blockage has already been taken by the CEI layer. Instead, it is to physically separate the highly oxidizing delithiated cathodes from the CEIs and the liquid electrolyte and to suppress continuous oxygen outgassing from the bulk of the oxide cathodes. This is consistent with the fact that the as-formed surface phase and good cathode coatings all have limited electrochemical activity and good stability over a wide range of anodic voltage ranges, and they do not release oxygen gas. For example, NiO, Co_3O_4, Al_2O_3, and AlF_3 are not redox-active within the spanned voltage range of a cathode, $LiNi_{0.5}Mn_{1.5}O_4$ shows limited capacity below 4.6 V (vs Li^+/Li, thus being suitable as a coating material for high-voltage $LiCoO_2$), and CoB_x forms strong Co–O/B–O bonds at its interface with the cathode and with any outgassing oxygen species.

The oxygen release and side reactions consume the liquid organic electrolyte, which is often the most precious component inside practical full cells. Overgrowth of CEIs and the cation-densified surface phase would eventually use up the electrolytes and lead to significant impedance growth because Li^+ can no longer be transported between the two electrodes. Furthermore, the side reactions cause TM dissolution (reduced TM ions, such as Mn^{2+}, Ni^{2+}, and Co^{2+}), which can migrate to and attack the surface of the anode.[108] It is known to destabilize the passivating SEIs and result in continuous side reactions on the anode side and overgrowth of SEIs, which consumes both the electrolyte and the lithium inventory.[109−112]

Beyond chemical and electrochemical effects, the cathodes suffer from mechanical and microstructural degradations. When a layered cathode is charged, there are volume expansion/shrinkage and anisotropic changes in the lattice parameters. For example, when NCM811 is charged from 3.0 to 4.4 V (vs Li^+/Li), the a-axis lattice parameter shrinks by 2%, and the c-axis lattice parameter first increases by 2% and then shrinks by 3% from the peak value. Correspondingly, the anisotropy ratio (c/c_0)/(a/a_0) first increases by 4% and then shrinks by 3–4%.[113,114] (Here, a and c denote the stress-free lattice parameters at different voltages, and a_0 and c_0 denote the ones in the fully discharged state.) As more Li is extracted from the Li layer, the interlayer bonding becomes weaker, which triggers sliding between TM slabs and bulk phase transformations. (Note the bulk phase transformations from TM slab sliding are mass-conserving and only involve symmetry change.) For single-crystalline layered cathodes (e.g., $LiCoO_2$), the uniform eigenstrain (i.e., stress-free strain caused by lithiation/
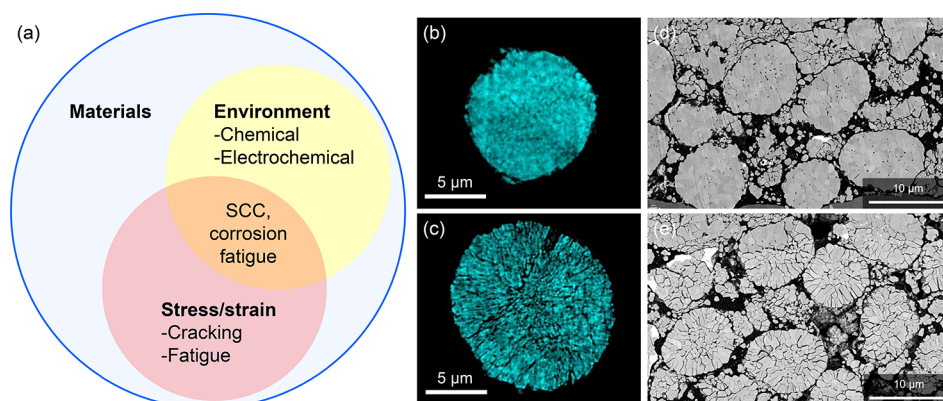
Figure 5. (a) Schematic showing that SCC requires both stress/strain and corrosion from the environment. In comparison, pure mechanical cracking and fatigue can be caused by stress/strain only. Corrosion fatigue also requires both stress/strain and corrosion but arises from cyclic dynamic mechanical loading, while SCC arises primarily from static mechanical loading. Cross-sectional tomography images of NCM811 showing cycling in (b) a "good" liquid electrolyte with suppressed environmental corrosion can mitigate SCC and maintain integrity, while cycling in (c) a "bad" electrolyte with intensive side reactions causes extensive cracking. Reproduced with permission from ref 114. Copyright 2021 The Author(s) under exclusive license to Springer Nature. Cross-sectional scanning electron microscope (SEM) images of NCM811 showing (d) mitigated SCC with cathode surface coating and grain boundary infusion and (e) extensive cracking without the coating and infusion. Reproduced with permission from ref 79. Copyright 2021 The Author(s) under exclusive license to Springer Nature.
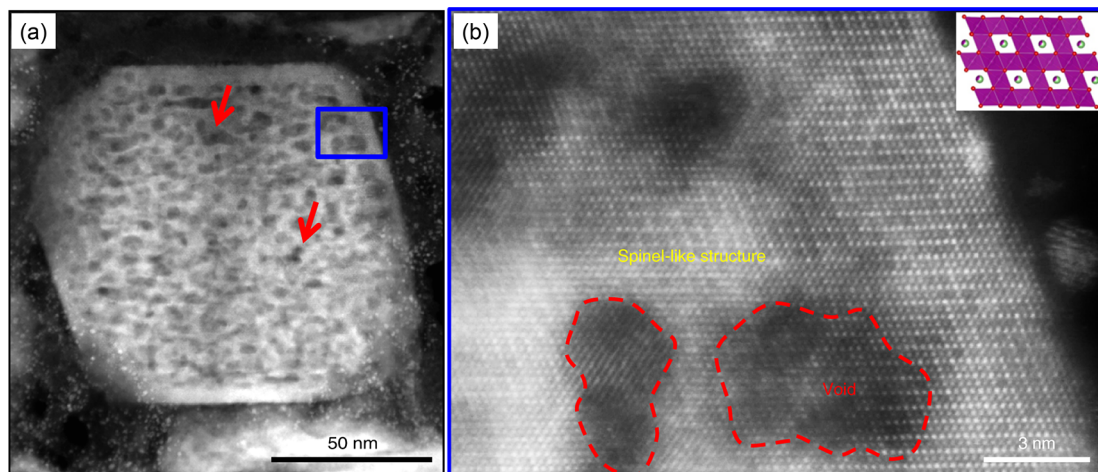

Figure 6. (a) Extensive cavitation in the bulk lattice and (b) bulk phase transformation from layered to spinel structure in $Li_{1.2}Ni_{0.2}Mn_{0.6}O_2$ after 300 cycles at 0.1 C between 2.0 and 4.8 V (vs Li^+/Li). Reproduced with permission from ref 119. Copyright 2019. This is a U.S. government work and not under copyright protection in the U.S.; foreign copyright protection may apply.

delithiation chemical expansion), and bulk phase transformations (accompanied by abrupt changes in lattice parameters) seem to be manageable and do not cause severe intragranular cracking within each particle. Upon electrochemical cycling, the cyclic straining and phase transformations could cause fatigue and microcracks. While electrochemically degraded cathodes typically show more microcracks and the suppressed bulk phase transformations (e.g., by lattice doping) often result in better cycling stability, interpreting such correlation as the causation of the electrochemical degradations requires extra caution, as the relatively low density of microcracks is unlikely to dramatically affect the percolating diffusion pathway of Li^+ and electrons in a single crystal. One possible explanation is that while the electrochemically active single-crystal lattice can accommodate the uniform eigenstrain, the inactive cation-densified surface phase and coatings cannot (SEI layer may not either). As a result, cyclic straining and interlayer sliding may crack the surface passivation, which results

in more side reactions and uncontrolled growth of the cation-densified surface phase as well as the SEIs.

The mechanical and microstructural degradations are more pronounced in polycrystalline layered cathodes (e.g., NCM and NCA), where intergranular cracking caused by strain mismatch and stress concentration at grain boundaries is a major degradation mechanism. (Intragranular cracking can also form inside the primary particle of polycrystalline layered cathodes after prolonged cycling.) It not only causes losses of electrical contacts between the primary particles (grains) but also generates many unprotected fresh surfaces, thus resulting in extensive side reactions. The intergranular cracking had been mostly attributed to a purely stress-driven event, whereas chemical/electrochemical corrosion later follows at the generated fresh surfaces after the cracking. However, in the literature, modified cathode and/or cathode−electrolyte interactions such as surface coatings, grain boundary infusions, and good electrolytes and electrolyte additives have been reported to relieve the cracking, including in deep-charge cycling (e.g., with
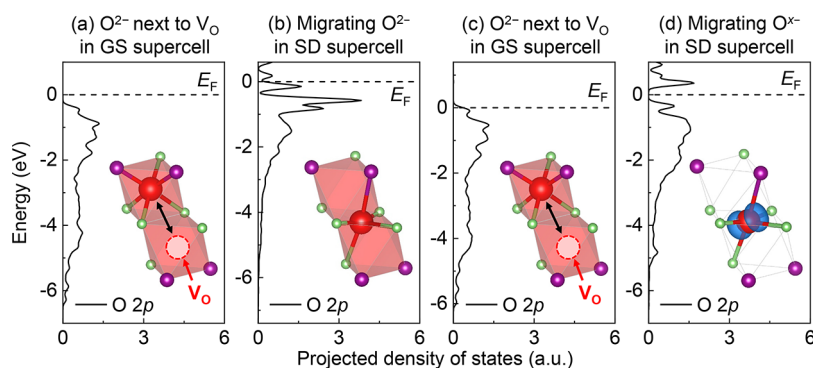
Figure 7. (a) Projected DOS of a to-be-migrating O^{2-} next to an oxygen vacancy V_O in the ground-state (GS) supercell before the migration in model A. (b) Projected DOS of a migrating O^{2-} in the saddle-point (SD) supercell of the migration in model A. (a) Projected DOS of a to-be-migrating O^{x-} next to a V_O in the GS supercell before the migration in model B. (b) Projected DOS of a migrating O^{x-} in the SD supercell of the migration in model B. The energies of the y axis were aligned using the band center of O $2p$ states of the nonmigrating lattice oxygen ions in the supercell. (a−d) Insets: Schematic local structures. (d) Inset: Electron cloud in blue denoting the unoccupied states (i.e., hole states) with 0.006 electron/Bohr^3 iso-charge-density. Reproduced with permission from ref 141. Copyright 2022 Elsevier.

an upper cutoff voltage of 4.7 V vs Li$^+$/Li for NCM811).[79,114−117] It indicates that the stabilized cathode−electrolyte interface and mitigated chemical corrosions (e.g., oxygen loss) suppress cracking. This is despite the fact that the same bulk redox, lattice expansion/shrinkage, and grain boundary mismatch straining take place in the polycrystalline cathodes. In addition, unlike mechanical cracking for brittle oxides, most cracks in polycrystalline cathodes tend to form after extended cycling, i.e., after cyclic loading. Based on these experimental observations, we recently proposed that the intergranular cracking is, from the beginning, a stress corrosion cracking (SCC, Figure 5) process,[118] and it involves both the mechanical stress/strain and the chemical interactions between the charged cathode and the electrolyte. (Both SCC and corrosion fatigue rely on simultaneous environmental and mechanical stressing, and their difference lies in static vs cyclic dynamic mechanical loading. A definite assignment to SCC and/or corrosion fatigue requires more experiments on the cracking behaviors at different charge/discharge rates to mimic the strain rate dependence and during constant-voltage floating tests to mimic static mechanical loading conditions.) In fact, the two are closely coupled, as the concentrated stress (especially tensile stress) would accelerate the corrosion process, and continuous side reactions would corrode the grain boundaries, cause materials loss (oxygen loss and TM dissolution), and offer thermodynamic and kinetic advantages to the initiation and propagation of SCC. The proposed SCC mechanism offers new insights into the coupled electrochemomechanics of oxide cathodes under extreme electrochemical conditions and the mitigation strategies.

In addition to the above, cavitation in the lattice (Figure 6a) and bulk phase transformation from layered to spinel structure (Figure 6b) have been reported for LRNCM.[43,119] Figure 6a shows an extreme case where numerous cavities formed throughout the entire particle of cycled $Li_{1.2}Ni_{0.2}Mn_{0.6}O_2$.[119] These lattice cavities were initially formed close to the surface of the cathode particles in the early cycles and then proceeded inside with prolonged cycling. While there is not a clear answer on whether these cavities are voids or oxygen bubbles, their formation during room-temperature battery cycling definitely requires mass flow and thus lattice diffusion of oxygen anions, which should be the slowest moving species in layered cathodes. Meanwhile, the phase transformation involved is also non-

conserved in oxygen. The transformed spinel structure has mixed LiM_2O_4 and M_3O_4 characteristics, both of which have M/O ratio $\geq 1/2$ that is higher than the original composition (M/O ratio of 2/5 for $Li_{1.2}Ni_{0.2}Mn_{0.6}O_2$). It thus indicates loss of oxygen in the transformed bulk lattice, which again requires lattice diffusion of oxygen anion. The lattice diffusion requires a point defect to form and migrate. A low defect formation energy for diffusion-mediated oxygen vacancy is not unexpected because the charged cathodes are not thermodynamically stable. Substantial lowering in oxygen vacancy formation energy from fully lithiated to highly delithiated cathodes has been reported for many layered cathodes (e.g., $LiCoO_2$, $LiNiO_2$, $Li-Ni_{0.33}Co_{0.33}Mn_{0.33}O_2$, and $Li_{1.25}Ni_{0.17}Mn_{0.58}O_2$) which is not unique for LRNCM.[119−121] A more striking yet less discussed aspect is the anomalously high room-temperature oxygen mobility in the lattice, which will be discussed in detail in the following section.

Lastly, it is important to acknowledge the spatial heterogeneity both at the cathode particle level and at the composite electrode level.[122−124] The heterogeneity depends on many factors such as the spatial distributions of active materials, conductive carbon, binder, and porosity, macroscopic defects in the electrode, the shape and crystallography of cathode particles, and the spatial uniformity of the surface passivation. It affects the transport of Li$^+$ and electrons, as well as the local chemical potential of Li^0.[125−127] With a large spatial heterogeneity either from cathode processing or after extended cycling, such as detachment of some particles from the electron percolating network or even wholesale detachment of the electrode from the current collector, these particles would be electrically insulated and become electrochemically inactive. What is worse, the charge/discharge current density calculated from the nominal active material loading would only be loaded on the active ones, which is equivalent to a high-rate cycling condition and result in accelerated degradations. The heterogeneous charge distributions can now be mapped by advanced characterization techniques, and degraded cathodes indeed show more spatially distributed redox behaviors (e.g., the valence of the redox-active TM elements) within each particle and across different ones.[128−130] The dynamics of particle network in composite battery cathodes, and the collective vs asynchronous activities have been reported to be the key to the full utility of cathode capacity and long-term cyclability.[131] Such a multiscale

understanding of the microstructure is critical to the improvement of the processing techniques and the mitigation of the correlated cathode heterogeneity and degradations.

5. OXYGEN MOBILITY

The problem of lattice oxygen mobility was investigated by Lee and Persson[132] with density functional theory calculations in Li_2MnO_3, which is a model layered structure with oxygen redox activity and the parent structure of LRNCM. Assuming an oxygen vacancy diffusion mechanism, the migration barrier (i.e., the energy barrier of an exchange event between an oxygen vacancy and a neighboring oxygen ion) was calculated to be 3.9 eV in Li_2MnO_3, 2.0 eV in $Li_{1.5}MnO_3$, 0.9 eV (for O^-, lower than 2.3−4.0 eV for O^{2-} migration at the same composition) in $Li_{1.0}MnO_3$, and 2.1 eV in Li_0MnO_3. Lee and Persson[132] concluded that the 0.9 eV migration barrier indicates moderate oxygen mobility that may allow for oxygen diffusion at the surface with undercoordination, disordering, and strain but not in the bulk lattice. Nevertheless, it was later cited to support the anomalously high room-temperature oxygen mobility required to explain the experimental observations.[82,107,119] To shed more light on this subject, we conducted more detailed first-principles calculations by using the Vienna Ab Initio Simulation Package (VASP)[133−139] on oxygen migration in Li_2MnO_3 with oxygen redox activity using a supercell containing 32 Li, 16 Mn and 48 O (some ions were then removed to generate point defects of interest).[140,141]

To simplify the matter, we consider an oxygen vacancy mediated migration across the Li layer (inset of Figure 7a, plotted using VESTA[142]). Before and after the migration event, the oxygen ion is 6-fold coordinated in an octahedron with two Mn and four Li. During the migration event, the oxygen ion passes through a high-energy saddle point near the shared edge of the two neighboring OMn_2Li_4 octahedra. Considering the occupancy of the two Li at the shared edge and the possible anion redox state (here to simulate the oxidized oxygen ion O^{x-}, $0 < x < 2$, we added one hole into the Li_2MnO_3 supercell and the structural relaxations would determine whether it is a delocalized or localized oxygen hole state), there are six possible models for oxygen ion migration: model A, O^{2-} exchange with a +2 charged oxygen vacancy V_O^{2+} and with no lithium vacancy on the shared edge; model B, oxidized oxygen ion O^{x-} exchange with V_O^{2+} and with no lithium vacancy on the shared edge; model C, O^{2-} exchange with V_O^{2+} and with one −1 charged lithium vacancy V_{Li}^- on the shared edge; model D, O^{x-} exchange with V_O^{2+} and with one V_{Li}^- on the shared edge; Model E, O^{2-} exchange with V_O^{2+} and with two V_{Li}^- on the shared edge; and model F, O^{x-} exchange with V_O^{2+} and with two V_{Li}^- on the shared edge. As shown in Table 1, the migration barrier is insensitive to V_{Li}^- (models A, C, and E give similar values, and models B, D, and E give similar values) but strongly affected by the redox state, and the migration barrier of O^{x-} (2.32−2.37 eV, models B, D, and F) is ~0.7 eV lower than that of O^{2-} (3.00−3.13 eV, models A, C, and E), despite the minor redox introduced (one electron per supercell, or ~0.02 electron per O).

Careful inspections of the Bader charge[143] of the migrating oxygen ion reveal interesting features. First, at the ground state before the oxygen ion migrates, the added hole in models B, D, and F tends to be delocalized (due to insufficient lattice distortions to render hole localization on some "special" oxygen ions) and the Bader charge of the to-be-migrating oxygen ion is similar to the corresponding case without the extra hole. Its

Table 1. Defect Configuration, Calculated Migration Barrier, and Bader Charges of Migrating Oxygen Ion at the Ground State before Migration and at the Saddle Point of Migration in Li_2MnO_3

Model	Defect configuration	Migration barrier (eV)	Bader charge (e) Ground state	Bader charge (e) Saddle point
A	O^{2-} exchange with V_O^{2+}	3.00	7.41	7.35
B	O^{x-} exchange with V_O^{2+}	2.33	7.40	7.05
C	O^{2-} exchange with V_O^{2+}, with one V_{Li}^-	3.13	7.32	6.96
D	O^{x-} exchange with V_O^{2+}, with one V_{Li}^-	2.37	7.25	6.92
E	O^{2-} exchange with V_O^{2+}, with two V_{Li}^-	3.09	7.23	6.73
F	O^{x-} exchange with V_O^{2+}, with two V_{Li}^-	2.32	7.14	6.77

Bader charge slightly decreases as the number of V_{Li}^- on the shared edge increases due to the electrostatic interactions between the negatively charged V_{Li}^- and the hole state (unoccupied electron state). Second, at the saddle point of migration, the added hole in models B, D, and F tends to localize on the migrating oxygen ion, causing ~0.3−0.4 e decrement in Bader charge. This indicates the saddle-point oxygen ion prefers an oxidized state. Because O^{x-} has lower absolute valence ($x <$ 2) and smaller size than fully ionized O^{2-}, the charge transfer helps to lower the migration barrier. Beyond the charge and size argument, the lower symmetry and weaker Mn $3d$−O $2p$ hybridization for the saddle-point oxygen ion raise the energy of its nonbonding orbitals above the Li−O−Li redox state, thus favoring hole localization and relaxations to lower the electronic energy (Figure 7). Such electronic structure relaxation comes from the extreme saddle-point local structure of the migrating oxygen ion, which has few Mn neighbors and minimal Mn $3d$−O $2p$ hybridization. It also has general insights on enhanced mobility of cations and anions in the heavily oxidized state as we reported.[141] Third, in the case of models C and E, where no extra holes were added to the supercell and all oxygen ions should be −2 charged, there is also a substantial decrement in the Bader charge of the migrating oxygen ion at the saddle point. We found that this is due to the existence of V_{Li}^-, which causes poor charge screening of the saddle-point oxygen ion. To better screen the charge and to lower the system energy, as the oxygen ion migrates to the saddle point, it donates electron to neighboring Mn following the reaction

$$O^{2-}(\text{ground state}) + Mn^{4+}(\text{lattice})$$
$$= O^{x-}(\text{saddle point}) + Mn^{(2+x)+}(\text{lattice}) \quad (4)$$
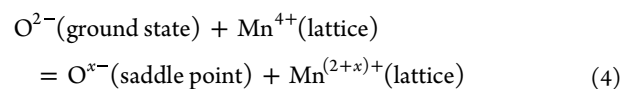
However, it does not lower the migration barrier because the exotic charge transfer in eq 4 costs energy. Summarizing the above three observations, one may expect higher mobility if the oxygen ion gets oxidized and the charge transfer does not cause additional penalty. This requires that the Fermi level of the system lies at or below the top of the O $2p$ band.

With the understanding above, we expect a further lowered migration barrier when more Li gets removed from Li_2MnO_3. We calculated the migration barrier of an oxygen ion in $Li_{0.81}MnO_3$ (removing 19 Li out of 32 Li in the supercell, corresponding to 273 mAh/g capacity, which is similar to that of LRNCM). For three converged calculations, we obtained migration barriers of 0.59, 0.62, and 0.76 eV and found

consistent Bader charge decrement (∼0.2 e) of the migrating oxygen ion at the saddle point compared to the ground state. As oxygen diffusion would proceed percolatively along the path with the lowest migration barriers, we believe the effective migration barrier would be ≤0.6 eV for oxidized oxygen ions in LRNCM, which is low enough for active room-temperature long-range diffusion in the bulk lattice. This offers plausible explanations for the experimental observations. Furthermore, one may rationally argue that higher oxygen mobility is triggered when more oxygen redox is used, so the usage of TM and oxygen redox in HACR paradigm should be balanced to achieve high capacity and energy density while not invoking long-range oxygen diffusion (to lose oxygen through the surface or to form bubbles in the lattice) and massive lattice reconstruction. With high oxygen mobility, on the good side, diffusional processes such as creep could take place to release the stresses in the lattice and at the grain boundaries. This could avoid brittle fracture of the oxide particles. On the bad side, long-range oxygen loss from particle interior to the surface becomes possible. This could result in bulk phase transitions from layered structure to cation-densified spinel and rocksalt structures and cavities (voids and/or oxygen bubbles) in the particle interior, which agree with the experimental observations.

We also conducted similar calculations in $LiCoO_2$ that primarily operates on TM redox but not on oxygen redox. (A supercell containing 27 Li, 27 Co and 54 O was used without counting the generated point defects.) We obtained migration barriers of 2.90 eV for model A, 3.02 eV for model B, 3.38 eV for model C, 3.59 eV for model D, 3.21 eV for model E, and 3.37 eV for model F, which are not affected by the extra hole added to the supercell. This is understandable because the added hole would cause oxidation of Co^{3+} to Co^{4+}, which lies at higher electronic energy than the O $2p$ states. With a Fermi level away from the top of the O $2p$ states, delithiation of $LiCoO_2$ is not expected to lower the migration barrier of oxygen ion either. This is also confirmed by our calculations in highly delithiated $LiCoO_2$, where three converged calculations in $Li_{0.30}CoO_2$ (corresponding to 192 mAh/g capacity) give migration barriers of 3.05, 3.34, and 3.47 eV. Therefore, consistent with the general insights discussed above, room-temperature oxygen mobility in the lattice should be very low and insensitive to the depth of charge in TM redox-based layered cathodes. Nevertheless, due to defective atomic structure, distinct redox chemistry and bandgap narrowing of surfaces and grain boundaries, oxygen mobility at these two-dimensional planar defects is sufficiently high to allow for long-range transport in TM redox-based layered cathodes. This is supported by the following experimental observations. Figure 8a shows an atomically sharp twin boundary that separates two grains, both with well-ordered layered lattice in $LiNi_{0.76}Mn_{0.14}Co_{0.10}O_2$ before cycling.[30] Figure 8b shows the local structure near a twin boundary in cycled Li-$Ni_{0.76}Mn_{0.14}Co_{0.10}O_2$, where NiO-like rocksalt phase forms between the two neighboring grains. Recall that the phase transformation from layered phase to cation-densified NiO-like rocksalt phase is oxygen nonconserving and must involve oxygen loss. So there is active oxygen diffusion along the twin structure as well as the later-stage formed interface between the untransformed layered phase and the transformed NiO-like rocksalt phase, most likely in the charged state. Figure 8c−e show the local structures near the tip of an intragranular crack inside the primary particle of cycled NCM811, where NiO-like rocksalt phase forms at the surface of the ∼1 nm wide crack as well as at the uncracked tip.[144] Following the same argument, it
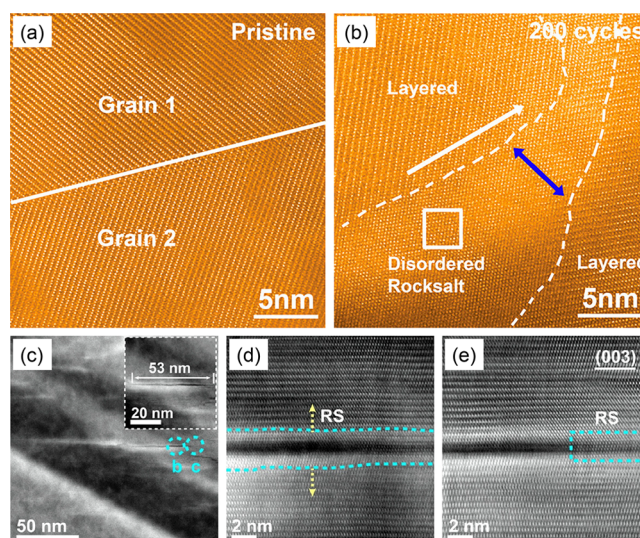

Figure 8. (a) An atomically sharp twin boundary in pristine $LiNi_{0.76}Mn_{0.14}Co_{0.10}O_2$ before cycling. (b) A thick layer of NiO-like rocksalt phase forms between the two neighboring grains in cycled $LiNi_{0.76}Mn_{0.14}Co_{0.10}O_2$, replacing an "original" twin boundary. Reproduced with permission from ref 30. Copyright 2020 American Chemical Society. (c) Microstructure of cycled NCM811 showing intragranular cracking inside the primary particle. Formation of NiO-like disordered-rocksalt phase (d) at the surface of the crack and (e) at the lattice of the crack tip. Reproduced with permission from ref 144. Copyright 2020 Elsevier.

suggests active oxygen diffusion along the crack surface. As the particle has already cracked, oxygen molecules may readily form (no elastic energy penalty) and oxygen gassing through the nanoscale channel is also possible. Lastly, considering strong hybridizations between TM d and O $2p$ states, high-voltage cycling may also enhance oxygen mobility in TM redox-based layered cathodes. For example, voids/oxygen bubbles have also been observed near the surface of high-voltage $LiCoO_2$ cycled with an upper cutoff voltage of 4.6 V (vs Li^+/Li).[145] These are important considerations in order to understand and mitigate cathode degradations.

6. DAMAGE TOLERANCE AND SELF-HEALING

Oxide ceramics are perceived as typically brittle. This is because dislocations are difficult to nucleate/migrate, so there are no applicable plastic deformation mechanisms to release mechanical stress at room temperature. Yet the electrochemically active oxide cathodes discussed above can withstand the large anisotropic eigenstrains during charge/discharge as well as the abrupt structural changes during the slab-sliding induced bulk phase transformations. It shares some similarities with transformation plasticity but is more reversible in the sense that cyclic electrochemical load can be applied without heat treatment to recover the original phase before the transformation. With optimized compositions, good coating, and modified electrolytes, there is minimal cracking of the single-crystalline cathodes (e.g., $LiCoO_2$ and NCM) over a few hundred cycles. It indicates that the slab sliding is reversible with minimal structural damage to the crystal lattice of the micrometer-sized particles, and the damage accumulated over cyclic loading is not excessive. To enable sliding while suppressing cracking, the bonding between two neighboring TM slabs should be anisotropic, weak in shear and strong in the opening. Such peculiar mechanical properties
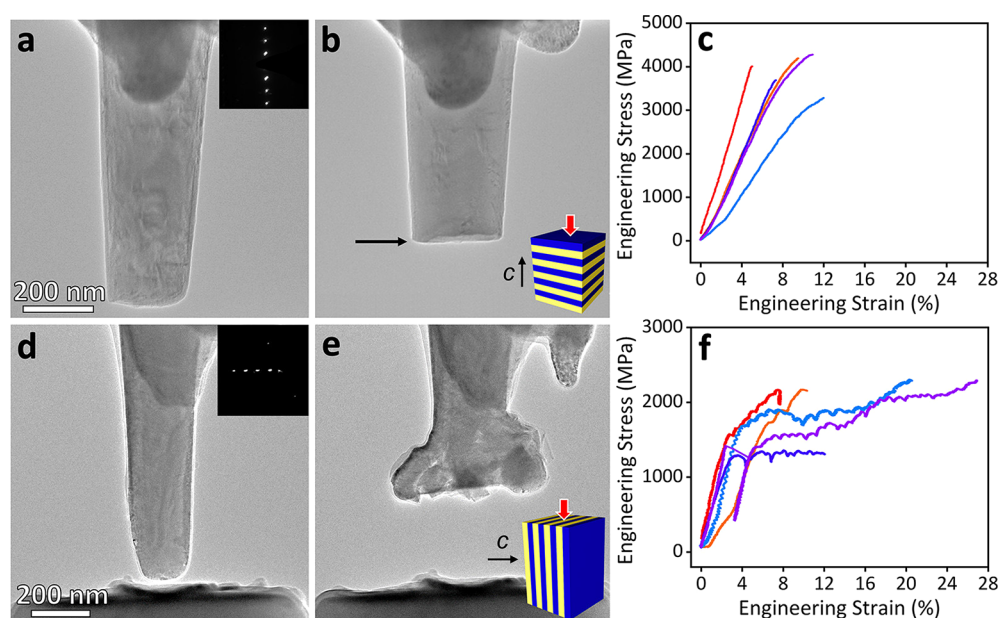
Figure 9. In situ compression test of a single-crystalline pillar of charged $Na_{0.7}Ni_{0.3}Mn_{0.6}Co_{0.1}O_2$. (a−c) Morphology (a) before and (b) after the compression perpendicular to the basal plane and (c) the corresponding stress−strain curves from multiple tests. (d−f) Morphology (d) before and (e) after the compression along the basal plane and (f) the corresponding stress−strain curves from multiple tests. Reproduced with permission from ref 146. Copyright 2021 American Chemical Society.
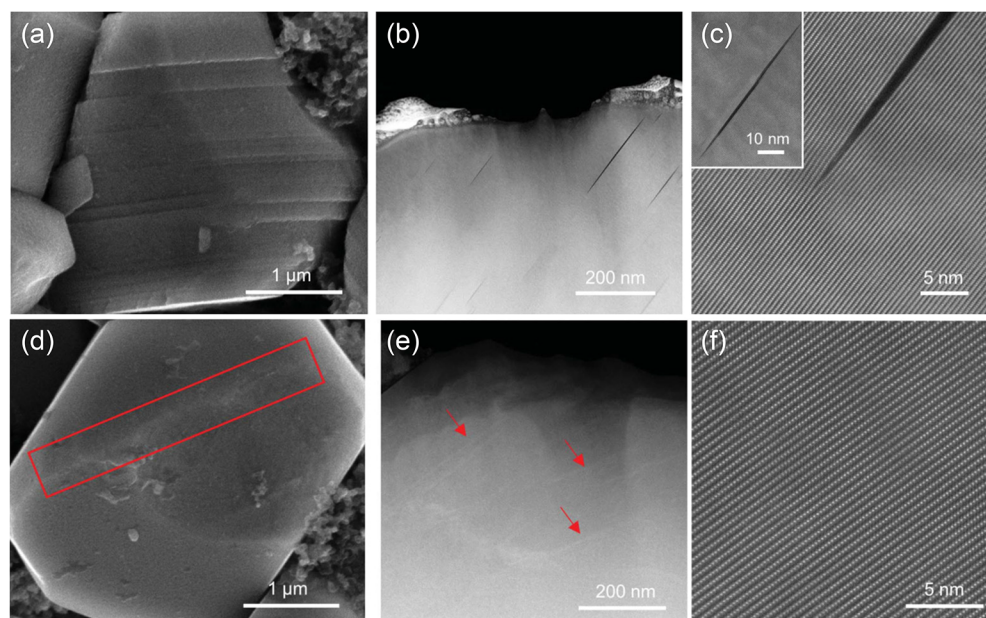

Figure 10. (a) SEM image of single-crystalline $LiNi_{0.76}Mn_{0.14}Co_{0.1}O_2$ charged to 4.8 V (vs Li^+/Li). (b,c) Scanning transmission electron microscopy (STEM) image of single-crystalline $LiNi_{0.76}Mn_{0.14}Co_{0.1}O_2$ charged to 4.4 V (in full cell and after cycling between 2.7 and 4.4 V for 120 cycles). (d) SEM image of single-crystalline $LiNi_{0.76}Mn_{0.14}Co_{0.1}O_2$ discharged to 2.7 V (after charging to 4.8 V, both vs Li^+/Li). (e,f) STEM image of single-crystalline $LiNi_{0.76}Mn_{0.14}Co_{0.1}O_2$ discharged to 2.7 V (in full cell and after cycling between 2.7 and 4.4 V for 120 cycles). Red arrows in (e) indicate trace marks for gliding inside the lattice. Reproduced with permission from ref 148. Copyright 2020 American Association for the Advancement of Science.

have been directly demonstrated by in situ compression tests of single-crystalline pillars of charged $Na_{0.7}Ni_{0.3}Mn_{0.6}Co_{0.1}O_2$, a layered cathode for sodium-ion batteries.[146] The compression perpendicular to the basal plane (i.e., the *ab* plane) in Figure 9a− c shows quasilinear stress−strain response, limited plastic deformation, and brittle fracture with a sharp fracture surface. In comparison, the compression along the basal plane in Figure 9d−f shows substantial plastic deformation, extensive nonlinear responses, and interesting flow-stress plateaus with ∼8−28%

plastic strain. The compressed pillar in Figure 9e is much shortened and extended along the lateral direction without observable cracks.

From an atomistic point of view, the slab sliding is not expected to be through rigid-body layer translation between neighbor TM slabs. Instead, it should be mediated by the glide of dislocations, i.e., the boundary between the transformed region and the untransformed region. This is the same argument as plastic deformation of a crystal takes place by dislocation glide at

much lower stress than that is required to simultaneously move a whole plane of atoms over another. While dislocations may nucleate at surfaces and dislocation glide does not rely on diffusion, the process involves lattice reconstruction and relaxation involving the oxygen ions. Therefore, softening of the oxygen ion sublattice should facilitate the nucleation and the gliding motion of dislocations. Thus, dislocation dynamics is expected to be more active when the layered cathodes are charged to higher voltage and especially when oxygen redox is activated. Using in situ Bragg coherent diffractive imaging technique, Singer et al.[147] tracked the three-dimensional displacement field inside primary cathode particles during cycling and calculated the dislocation density in $Li_{1.2}Mn_{0.533}Ni_{0.133}Co_{0.133}O_2$ and $LiNi_{0.80}Co_{0.15}Al_{0.05}O_2$ at different charge voltages. Consistent with our argument, the dislocation density in $Li_{1.2}Mn_{0.533}Ni_{0.133}Co_{0.133}O_2$ rapidly increases once the voltage plateau of oxygen redox is reached, and it is much higher in $Li_{1.2}Mn_{0.533}Ni_{0.133}Co_{0.133}O_2$ ($\sim 10^{10}$ cm^{-2}) than in $LiNi_{0.80}Co_{0.15}Al_{0.05}O_2$ ($\sim 10^9$ cm^{-2}) at 4.4 V (vs Li^+/Li). We may call this phenomenon HACR-lubricated plasticity.

In addition to the peculiar plasticity, self-healing of generated intragranular microcracks in single-crystalline cathodes has been reported by Bi et al.[148] Figure 10a−c shows the cross-sectional images of single-crystalline $LiNi_{0.76}Mn_{0.14}Co_{0.1}O_2$ in charged states, where slab sliding created steps at the surface and microcracks in the lattice. Surprisingly, as shown by Figure 10d− f, when the cathode was fully discharged, not only the surface steps were gone but also the microcracks were healed. The sliding slabs went back to their original locations, which largely recovered the original morphology of the single-crystalline particle and only left some trace features in the lattice without initiating visible damage. Similar observations, microcracking generation at high charged voltages and self-healing when fully discharged, have also been observed in its extended cycling between 2.7 and 4.4 V in full cells paired with graphite anode. Such a peculiar microcrack healing phenomenon has been directly visualized in $Na_{0.7}Ni_{0.3}Mn_{0.6}Co_{0.1}O_2$ by in situ TEM over repeated charge/discharge cycles.[146]

Unlike single crystals, the large strain mismatch and stress concentration at the grain boundaries of polycrystalline cathodes are more difficult to manage. For example, NCM811 undergoes $\pm 4\%$ change in the anisotropy $(c/c_0)/(a/a_0)$ during the charge/discharge. Using a Young's modulus of ~ 140 GPa,[149] it would lead to an unphysically large elastic stress of ~ 6 GPa if there are no inelastic relaxation processes involved at an uncracked grain boundary because the grain boundary is not an invariant-plane of the martensitic-like transformation, i.e., the grain-boundary length is not preserved across the two sides of the boundary.[114] (Here we only consider an imagined coherent strain-matching and the 6 GPa elastic stress does not account for the concentration factor at a crack tip. It readily suggests severe cracking of the ceramic particles, especially mode II and III cracking under shear.) For well-protected polycrystalline cathodes with good cycling stability, experiments show that many grain boundaries still remain intact after extended cycling. Therefore, significant inelastic grain boundary sliding is very likely to happen to preempt the huge stress build-up and cracking during the electrochemical cycling, which is again surprising for ceramic materials. The peculiar plasticity, microcracking self-healing, and grain boundary sliding in electrochemically active cathode particles all point to a dynamic, reversible bond breaking and reforming process similar to a

tribochemical effect.[150] We argue that the key lies in the enhanced CCAM at higher voltages, as well as the conservation of the species at the local and global levels, where the loss of oxygen and TM elements would result in irreversibility. In other words, with the participation of active oxygen redox and dynamic changes in the TM-O bonding characteristics, reversible structural changes are facilitated and irreversible ones (e.g., in-plane microcracking in the lattice) are suppressed. The HACR-lubricated plasticity, grain boundary sliding, and "miraculous" self-healing reviewed in this section are all consistent with CCAM mentioned at the end of section 3 that are only activated at voltages far from the OCV. It is consistent with the experimental observations and the proposed SCC mechanism applied to both intragranular and intergranular cracking. This is also the key to degradation mitigations, as shall be discussed in the following section.

7. STRATEGIES TO MITIGATE DEGRADATIONS

Doping is one of the most frequently practiced methods in mitigating cathode degradations. Uniform bulk doping is often achieved by high-temperature annealing, as many elements have considerable solubilities in the layered cathodes. It is used to tune bulk redox chemistry and to suppress the abrupt slab-sliding induced bulk phase transformations (by pillar elements such as Mg^{2+} and Ni^{2+} that substitute Li^+ in the Li layer). As we discussed before, the suppressed bulk phase transformations result in not only less mechanical and microstructural degradations of the oxide but also less damage to the as-formed surface passivation. The combined outcome is less surface side reactions, less SCC, more reversible slab sliding, and more robust microstructure. However, interpreting the benefits of a trace amount of bulk doping (e.g., <1% of the TM amount) demands extra caution, as it is not expected to significantly alter the bulk behavior. Instead, the working mechanism should be primarily from its segregations at surfaces and grain boundaries and the modified cathode−electrolyte interactions. For example, it has been reported that 0.1 wt % Ti segregates at the surface and grain boundaries of Ti, Mg, and Al codoped high-voltage $LiCoO_2$, which stabilizes the surface oxygen and improves the cycling;[52] Al segregation at the surface of both the secondary and primary particles of $LiNi_{0.92}Co_{0.06}Al_{0.02}O_2$ has also been reported to stabilize the cathode−electrolyte interface accompanied by the formation of more stable CEIs.[151] These thermodynamically driven interfacial segregations in bulk doping practices echo the ideas of surface doping[152,153] and constructing TM concentration gradients[154,155] that are achieved by special synthesis techniques with built-in chemical gradients and then kinetically suppressing the high-temperature homogenization.

With regard to the microstructure design, the coprecipitation technique has been widely used to produce high-reactivity hydroxide or carbonate precursors for NCM, NCA, and LRNCM with atomically uniform elemental distributions and with self-assembled secondary particles (~ 10 μm in diameter) to improve the packing density of cathode-active materials in battery electrodes. The lowered lithiation temperature that suppresses Li/Ni cation mixing is critical to the synthesis of high-quality Ni-rich layered cathodes. However, the self-assembled secondary particles can be cracked along grain boundaries in the electrode calendering process (pure mechanical cracking) and during the electrochemical cycling (SCC), which is a major degradation mechanism. To improve the grain boundary cohesion, lower the anisotropic strain mismatch during charge/discharge, and tune the internal stress
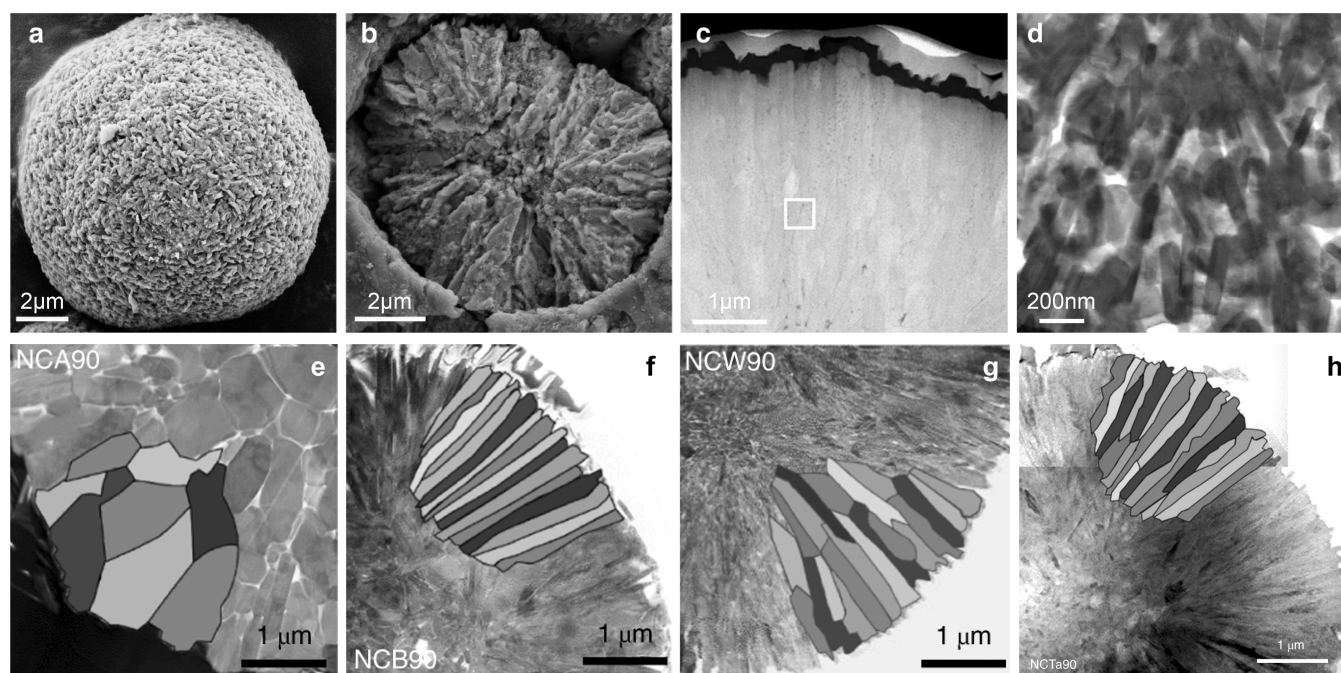
Figure 11. (a−c) Microstructure of secondary particles of Ni-rich layered cathode with radially aligned primary particles. Reproduced with permission from ref 156. Copyright 2020 The Author(s). (d) Rod-like primary particles in concentration gradient Ni-rich layered cathode. Reproduced with permission from ref 154. Copyright 2012 Nature. (e−h) Microstructure of Ni-rich layered cathodes synthesized using the same $(Ni_{0.91}Co_{0.09})(OH)_2$ precursors but adding (e) Al, (f) B, (g) W, or (h) Ta with 1/99(Ni+Co) mole amount. Reproduced with permission from ref 157. Copyright 2020 The Author(s) under exclusive license to Springer Nature.

distribution, grain-textured secondary particles with radially orientationally aligned primary particles (Figure 11) have been produced with better mechanical and microstructural stability. Such a specially designed microstructure is typically obtained by standard lithiation process (mixing with Li salts followed by heat treatment) on specially processed solid precursors.[156] Clearly, it requires much knowhow in the coprecipitation, which sets an initial condition for the microstructural evolution during the complicated process of hydroxide/carbonate decomposition, lithiation, grain growth, and texture development during the heat treatment. In addition, a minor addition (∼1% over the TM amount) of some elements (e.g., B, W, and Ta) has been reported to slow down the grain growth and substantially alter the texture produced.[157] These elements, either covalently bonded with O with short bond lengths (as is the case for B) or too high in valence to substitute TM ions (as is the case for Ta^{5+} and W^{6+}), are expected to have low bulk solubilities in the layered cathode. As a result, they should have a strong preference to segregate at grain boundaries, which lowers the grain boundary energy and mobility and results in slower grain growth.

A complete solution to the intergranular cracking problem is to synthesize single-crystalline cathodes. It allows higher pressure to be used in the cathode calendering without cracking the particles, which increases the electrode density and the volumetric energy density and decreases the specific surface areas, thus giving fewer side reactions. Historically, micrometer-sized single-crystalline $LiCoO_2$ and $LiMn_2O_4$ are very successful, and the lesson further drives the development of single-crystalline Ni-rich layered cathodes and LRNCM.[158−161] To produce single-crystalline Ni-rich layered cathodes with good electrochemical performance, the lithiation temperature needs to be kept relatively low (no more than 800 °C for NCM811 and lower for higher Ni content) to minimize Li/Ni cation mixing.

As we discussed above, the amount of Li/Ni cation mixing is an indicator of both the bulk redox activity (a too high amount such as >5% suggests poor Li^+ diffusion kinetics in the lattice) and the amount of surface impurity phase (resistive NiO-like rocksalt phase). Achieving a low Li/Ni cation mixing (e.g., <3%) is a necessary but insufficient condition for good electrochemical performance, and further characterizations and optimizations on the cathode surface are required. Two critical insights have been gained in the practices to produce single-crystalline Ni-rich layered cathodes from coprecipitated precursors.[158,159] First, not all of the precursors work equally. With the same Li salts and lithiation conditions, different precursors show different particle growth kinetics and different morphology of the final product. It again points to the key role of precursors in the synthesis. Segregating impurities may also matter and need to be minimized, as now we are in the opposite situation of producing fine radially aligned primary particle texture and actually want a grain to grow faster once nucleated. Second, a two-step heat treatment schedule is helpful by first heating to a higher temperature (∼950 °C) to obtain single-crystalline particles and then annealing at a lower temperature (∼800 °C) to recover the Li/TM order and reduce the amount of Li/Ni mixing. This method is known to work, yet the first-step temperature needs to be carefully chosen; otherwise, the second step would not be able to recover the preferred layered structure in the bulk and at the surface.

Coating is another widely practiced method to mitigate cathode degradations. While a thin protective coating of electrochemically and catalytically inert compounds (e.g., Al_2O_3, ZrO_2, Li_3PO_4, and AlF_3) is helpful, it is difficult to achieve full surface coverage with a scalable synthesis method and to remain conformal during the electrochemical cycling. The task is even more difficult for polycrystalline cathodes, whose grain boundaries also need to be protected as they would
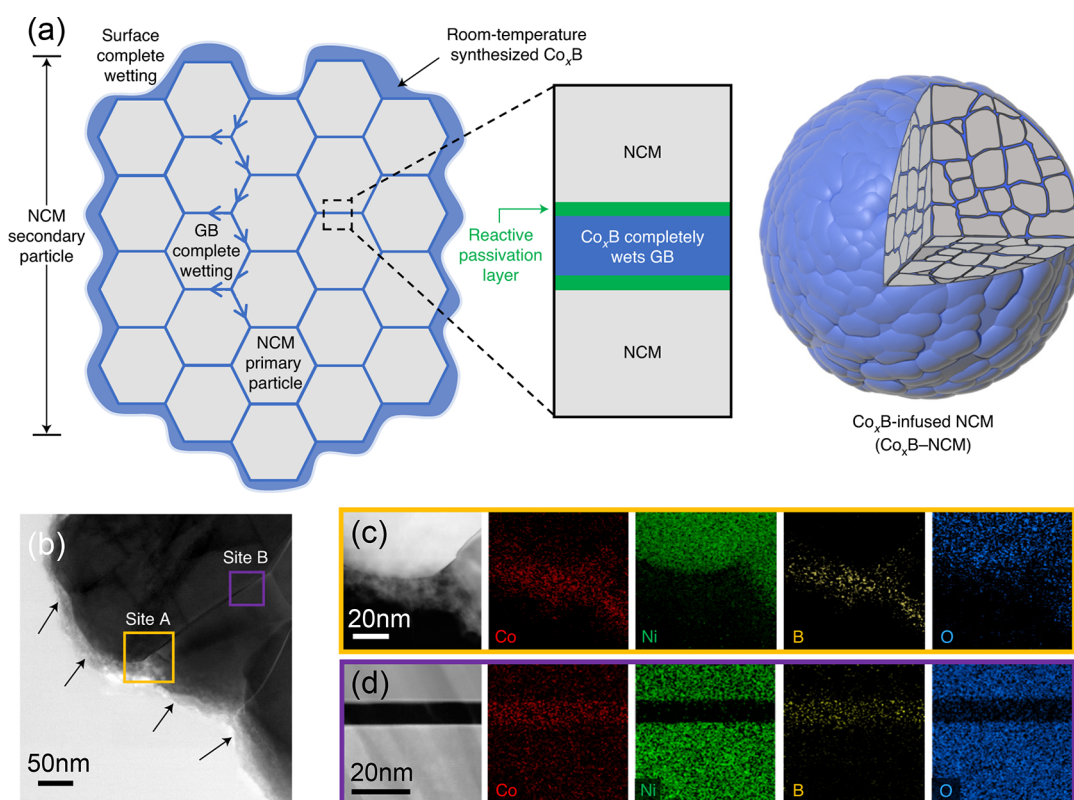
Chemical Reviews   pubs.acs.org/CR   Review

Figure 12. (a) Schematic coating-plus-infusion microstructure where Co_xB uniformly coats the surface of the secondary particle of NCM811 and infuses into the grain boundaries between the primary particles. (b) TEM images of cross-sectioned NCM811 coated and infused with Co_xB. (c) EDS of site A in (b) showing surface Co_xB coating. (d) EDS of site B in (b) shows Co_xB phase with a uniform thickness and perfectly wetted the grain boundary. Reproduced with permission from ref 79. Copyright 2021 The Author(s) under exclusive license to Springer Nature.

be exposed to the liquid electrolyte upon cracking. Such a challenging solid-on-solid wetting problem remains despite the fact that extensive wet-chemistry methods have been employed and optimized, followed by carefully controlled heat treatment. Gas-phase methods such as atomic layer deposition (ALD) and oxidative chemical vapor deposition have attracted much attention due to the capability to construct uniform conformal coatings with controlled thickness.[116,162−164] For example, Yan et al.[116] ALD-coated $LiNi_{0.76}Mn_{0.14}Co_{0.10}O_2$ with ~10 nm Li_3PO_4 at the surface of the secondary particles, and Li_3PO_4 infuses into the grain boundaries between primary particles after heat treatment at 600 °C for 2 h. The protection at both secondary and primary particle levels suppresses side reactions between the cathode and the electrolyte, intergranular cracking, and layered-to-spinel phase transformation at the surface. We recently reported a new wet-chemistry method to achieve full surface coverage and facile grain boundary infusion at room temperature without the need for any follow-up heat treatment.[79] The idea lies in reactive wetting, which provides a strong chemical driving force for the coating materials to be spread over the cathode surface and infusing deeply into the grain boundaries (Figure 12). We demonstrated the concept by treating NCM811 with amorphous cobalt boride Co_xB, a metallic glass that has a strong oxygen affinity and completely wets the surface and grain boundaries of the oxide cathode. (Note that a boride reactively wet the oxide, but a borate cannot.) It dramatically improved the rate capability and cycling stability by suppressing the side reactions and the microstructural degradation of the intergranular cracking. Atomistic simulations identified the critical role of strong selective

interfacial bonding, which supports a large chemical driving force for the reactive wetting mechanism as well as lowers the surface/interface oxygen activity. The Co_xB grain boundary phase also improves the mechanical strength of the cathode secondary particles, as supported by a higher "opening" strength at $Co_xB/LiNiO_2$ interface than at (104) face of bulk $LiNiO_2$ from first-principles calculations.

Similar to surface coating, it is helpful to directly engineer the near-surface composition and atomic structure of the cathodes. This is the design principle for concentration-gradient layered cathodes with a Ni-rich and Mn-poor inner core to increase capacity, with an Mn-rich and Ni-poor outer layer to increase high-voltage and thermal stability.[164,165] The idea originated from earlier investigations on core−shell structured layered cathodes,[166] and the technological advance avoids the sharp interface between the inner core and outer shell, thus offering a more robust microstructure. The desired TM concentration profiles can be continuously controlled by the coprecipitation parameters, and it has been demonstrated that the obtained profiles in the precursors can be well maintained in the final products with minimal homogenizations during the high-temperature lithiation process. In addition to the Ni versus Mn versus Co concentration gradients within a constant total TM concentration, we have recently reported a MoO_3 molten salt treatment to construct Li−TM concentration gradient in LRNCM, where the net TM concentration varies with the position, changing continuously from a Li-rich (Li replacing TM in the TM-layer) core to a Li-poor (TM replacing Li in the Li-layer) near-surface region.[82,107] As we explained in section 5, heavy usage of oxygen redox is accompanied by enhanced
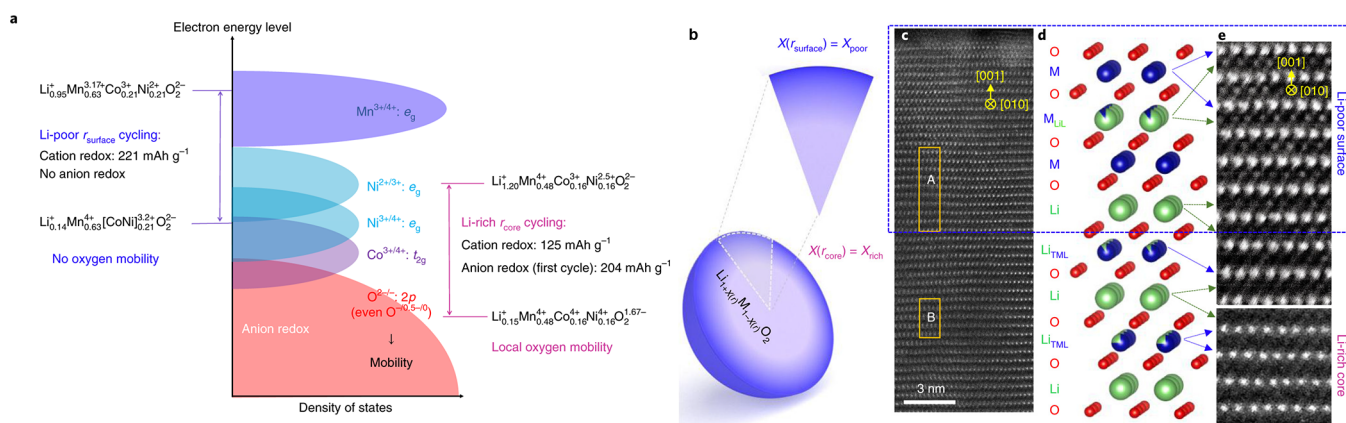
826

https://doi.org/10.1021/acs.chemrev.2c00251
Chem. Rev. 2023, 123, 811−833

Figure 13. (a) Schematic TM and oxygen redox couples of Li-poor surface composition $Li_{0.95}Mn_{0.63}Ni_{0.21}Co_{0.21}O_2$ and Li-rich bulk composition $Li_{1.20}Mn_{0.48}Ni_{0.16}Co_{0.16}O_2$. (b) Schematic particle with Li concentration gradient where deeper color indicates more TM and less Li. (c) STEM image from the inner core to the outer surface showing lattice coherency between the Li-poor (rectangle A) and Li-rich (rectangle B) regions. (d) Atomic structures of the Li-poor and Li-rich regions. (e) Higher-magnification STEM images showing TM in Li layer in the Li-poor region but not in the Li-rich region where the opposite happens. Reproduced with permission from ref 82. Copyright 2019 The Author(s) under exclusive license to Springer Nature.

oxygen mobility. Therefore, to suppress long-range oxygen diffusion and outgassing through the surface, one needs to lower the oxygen activity in the outer surface region. This is a challenging task, as the modified surface region needs to be sufficiently thick to block the oxygen outflux, and it needs to be uniformly applied to each cathode particle. We realized that MoO_3 can be beneficially used for such purpose because (i) Mo^{6+} has a low solubility in the layered structure, (ii) MoO_3 can extract Li_2O from LRNCM to become $Li_2Mo_4O_{13}$, $Li_4Mo_5O_{17}$, Li_2MoO_4, and their solid solutions, (iii) all compositions from MoO_3 to Li_2MoO_4 are in the liquid state at 800 °C (including a eutectic composition that melts at ~525 °C), thus providing a molten-salt bath during the heat treatment that reactively wets the oxide cathode particles and extracts Li_2O along the radial direction, and (iv) after the high-temperature molten salt treatment and cooling down to room temperature, the xLi_2O-$(1-x)MoO_3$ compound can be dissolved in water and washed away. It turns out the successfully produced Li concentration gradient (Li-rich core and Li-poor outer surface) has a smooth profile across ~10 nm depth from the surface (Figure 13) and transforms the original bulk composition $Li_{1.20}Mn_{0.48}Ni_{0.16}Co_{0.16}O_2$ to a new composition $Li_{0.95}Mn_{0.63}Ni_{0.21}Co_{0.21}O_2$ in the outer surface, with full epitaxy (lattice coherency). Note for Li-poor $Li_{0.95}Mn_{0.63}Ni_{0.21}Co_{0.21}O_2$, Ni is +2, Co is +3, and Mn has an average valence of +3.17, and their oxidations to +4 valence can provide 1.15 electron redox that is sufficient for charge compensation for electrochemical delithiation. Therefore, there should be no oxygen redox activity in the outer surface. This is the key to lowering global oxygen mobility (GOM), decreasing surface oxygen loss, and improving the cycling stability, including much suppressed voltage decay.

The development of advanced electrolytes is another way to stabilize the cathode−electrolyte interface and achieve better cycling stability. While the anodic stability window of the electrolyte is of critical importance, the cathode−electrolyte side reactions are more complicated than a simple charge transfer reaction (e.g., deprotonation reaction of the solvent) and involve many chemophysical processes. The interfacial stability heavily relies on surface passivation. In recent years, high-concentration electrolytes[167,168] have been demonstrated to reduce the free solvent activity at the cathode−electrolyte interface and produce

inorganic compound-rich surface passivation, which improves the cycling of both lithium metal anode and high-voltage cathodes, but the high price, high viscosity, and poor wettability with porous electrodes are issues to be addressed. For "normal" concentration electrolytes (e.g., with 1 M $LiPF_6$), fluorine-rich electrolytes with specially designed solvents have been reported to produce LiF-rich CEIs,[70,103] which is anodically stable and enables aggressive cathode chemistries such as $LiCoPO_4$ with an upper cutoff voltage of 5.0 V vs Li^+/Li. These advances point out the critical role of anion groups (of the Li salts) in constructing high-quality CEIs. To obtain more anion-derived CEIs, Li^+ needs to be weakly solvated and maintain a relatively strong correlation with the anion group in the electrolyte. This also leads to the development of anion-inspired solvent molecules and derivatives.[114,169−172] We recently reported the application of 1 m LiFSI in N,N-dimethyltrifluoromethane-sulfonamide (DMTMSA) electrolyte in constructing 4.7 V Li metal batteries paired with ultrahigh-voltage NCM811.[114] The 1 m LiFSI/DMTMSA suppresses cathode−electrolyte side reactions, SCC, TM dissolution, and impedance growth on the cathode side, Al current collector corrosion, and enables highly reversible Li metal stripping/plating with a compact morphology. In addition to the reasons discussed above, 1 m LiFSI/DMTMSA is relatively nonpolar, so inorganic salts generally have low solubilities in it. As a result, the side reaction products between the cathode and electrolyte and between Al/Al_2O_3 and LiFSI cannot be dissolved and diffuse away. Instead, they would quickly become supersaturated (e.g., at the nanochannel near the crack tip of SCC and at the surface of the Al current collector) and form a dense passivation layer (Figure 14).

Beyond liquid electrolytes, all-solid-state LIBs and Li metal batteries are under rapid development and show great promise for higher energy density and superior safety. As TM ions have no mobility to diffuse through the solid electrolyte layer, all-solid-state batteries no longer suffer from TM dissolution, migration and precipitation problem that limits the practical applications of cost-effective Mn-based cathodes. The integration of high-energy density cathodes in these all-solid-state devices is a promising area of study.
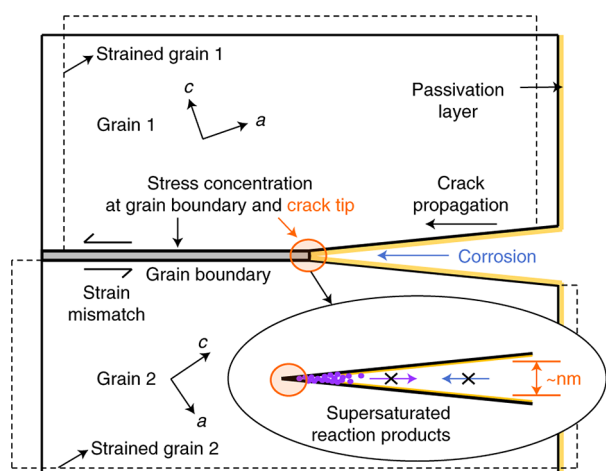
Figure 14. SCC at grain boundaries involves strain mismatch and chemical interactions between the cathode grain boundary/surface region and electrolyte and can be largely suppressed by less-reactive/corrosive electrolytes with supersaturated side reaction products at the surface and in the nanochannel near the intergranular crack tip. The dashed lines are schematics of the strained grains. Reproduced with permission from ref 114. Copyright 2021 The Author(s) under exclusive license to Springer Nature.

8. SUMMARY AND OUTLOOK

To summarize, we have presented an overview of the oxide cathodes, exemplified by the layered ones. The general insights on materials theory, chemistry, structure, electrochemomechanics, damage buffering, and degradation mitigations pave the way to further development of these materials, concerning both materials design and processing. A wide range of phenomena associated with cathode functioning, stability/instability, and degradation mitigations have an electronic origin, including formability of the oxide surface phase, redox potentials, anodic stability, and oxygen mobility. The chemical, electrochemical, and mechanical effects in electrochemically active oxides are clearly coupled, and a unified view of the electrochemomechanics is required to offer complete solutions to the cathode degradations. For example, the proposed SCC for intergranular cracking in polycrystalline cathodes and intragranular cracking in single-crystalline cathodes provides a fresh view and new strategies to mitigate the mechanical and microstructural degradations from the chemical stability perspective. Distinct electrochemical activities and degradation mechanisms have been identified for cathodes with vs without anion redox, which is related to oxygen redox enhanced CCAM, among other considerations. A better understanding of the thermodynamics and kinetics of HACR cathodes is required. Peculiar mechanical properties, damage tolerance, and self-healing phenomena have also been noted in layered cathodes, which not only buffer damage during battery cycling but also provide opportunities for these functional oxides to be used in many other applications. More fundamental research into the relationship between self-healing and exotic-valence-induced high cation and anion mobilities is needed to understand such surprising materials behaviors under dynamic electrochemical and extreme conditions, especially for high-capacity HACR cathodes.

With synergistic modifications, stabilized layered cathodes such as 4.6 V $LiCoO_2$, >4.5 V NCM811, and 4.8 V LRNCM should be able to deliver 850−1000 Wh kg^{-1} energy density at the cathode level over hundreds to thousands of deep-charge cycles under practical conditions. (High-voltage $LiCoO_2$ offers high volumetric energy density and would still be the preferred option for portable electronics, where volume is the most precious and the price is less of a concern.) The cathode modifications include the rational design of the chemical compositions, doping, microstructure, and coating. Challenges lie in both atomic-scale materials design with precision and large-scale synthesis/processing with uniformity, reproducibility, and reliability. Interfacial segregation of major and/or minor bulk doping elements is probably overlooked, and we suspect many bulk doping practices work by modifying the surface chemistry and cathode−electrolyte interactions. Polycrystalline microstructural design with chemical concentration gradients and radially aligned primary particles is useful, and it is in principle compatible with the next-level design of texture and grain boundary engineering, such as increasing the population of twin boundaries. Surface coating plus grain boundary infusion is clearly a better strategy than only covering the secondary particle surface, and its demonstration with a cost-effective method at the industry scale would be meaningful. In addition to the cathode itself, electrolytes clearly play a large role in stabilizing the cathode−electrolyte interface, which offers a drop-in solution to increase the energy density, cycling stability, and safety of the energy-dense batteries.

Looking forward, we call attention to a few other important directions. First, better characterization and computational techniques need to be developed and digested to get general materials insight that guides cathode processing and optimizations. Second, the sustainability issues need to be addressed. It is now a general trend to work on Co-free/lean cathodes, but Ni scarcity is also a concern. More abundant Mn and Fe should be used as the main cathode constituents. This requires new cathode designs, probably beyond layered ones. Third, new redox chemistries need to be explored to further increase the energy density. Questions such as the applicability of using high-voltage redox couples above 5 V (vs Li$^+$/Li) and reversible Fe^{4+}/Fe^{3+} or Mn^{6+}/Mn^{4+} redox couples remain to be answered. Lastly, most of the theoretical issues discussed in this review will manifest when a solid-state electrolyte is used. Certain aspects, such as electrochemomechanical degradation and self-healing will become ever more critical.

ASSOCIATED CONTENT

ⓈⒾ Supporting Information

The Supporting Information is available free of charge at https://pubs.acs.org/doi/10.1021/acs.chemrev.2c00251.

Oxide cathodes to self-healing (PDF)

AUTHOR INFORMATION

Corresponding Authors

Ju Li − *Department of Nuclear Science and Engineering and Department of Materials Science and Engineering, Massachusetts Institute of Technology, Cambridge, Massachusetts 02139, United States;* ⓞ orcid.org/0000-0002-7841-8058; Email: liju@mit.edu

Yanhao Dong − *State Key Laboratory of New Ceramics and Fine Processing, School of Materials Science and Engineering, Tsinghua University, Beijing 100084, China;* ⓞ orcid.org/0000-0003-1224-1015; Email: dongyanhao@tsinghua.edu.cn

Complete contact information is available at:
https://pubs.acs.org/10.1021/acs.chemrev.2c00251

Notes

The authors declare no competing financial interest.

Biographies

Yanhao Dong is an assistant professor in the School of Materials Science and Engineering at Tsinghua University. He obtained his B.S. degree in Materials Science in 2012 from Tsinghua University, and his M.S. degree in Materials Science in 2014, his M.S. degree in Applied Mechanics in 2015, and his Ph.D. degree in Material Science in 2017, all from University of Pennsylvania. His Ph.D. dissertation focused on cation diffusion in zirconia ceramics, covering from experiments of sintering and grain growth to continuum-level solution of transport and growth theory to atomistic simulations of defect energetics and kinetics. He then spent five years at Massachusetts Institute of Technology as a postdoctoral researcher working on interdisciplinary materials design, processing, microstructure, and degradation mechanisms. He received the Early Discovery Award, the Edward C. Henry Award, and the Morgan Medal and Global Distinguished Doctoral Dissertation Award from the American Ceramic Society, Acta Student Award from Acta Materialia, and Sidney J. Stein Prize from University of Pennsylvania. His current research interest is on advanced ceramics for structural and energy applications.

Ju Li has held faculty positions at The Ohio State University, the University of Pennsylvania, and is presently a chaired professor at MIT. His group (http://Li.mit.edu) investigates the mechanical, electrochemical, and transport behaviors of materials as well as novel means of energy storage and conversion. Ju is a recipient of the 2005 Presidential Early Career Award for Scientists and Engineers, the 2006 Materials Research Society Outstanding Young Investigator Award, and the TR35 award from *Technological Review*. Ju is included in Highly Cited Researchers lists from Thomson Reuters/Clarivate, Webometrics $h >$ 100 and research.com. He was elected Fellow of the American Physical Society in 2014, a Fellow of the Materials Research Society in 2017, a Fellow of the American Association for the Advancement of Science in 2020, and a Fellow of the Minerals, Metals and Materials Society in 2021. Li is the chief organizer of the MIT A+B Applied Energy Symposia, which aim to develop solutions to global climate change challenges with "A-Action before 2040" and "B-Beyond 2040" technologies.

REFERENCES

(1) Whittingham, M. S. The Role of Ternary Phases in Cathode Reactions. *J. Electrochem. Soc.* **1976**, *123*, 315−320.

(2) Mizushima, K.; Jones, P. C.; Wiseman, P. J.; Goodenough, J. B. Li_xCoO_2 ($0 < x \leq 1$): A New Cathode Material for Batteries of High Energy Density. *Mater. Res. Bull.* **1980**, *15*, 783−789.

(3) Whittingham, M. S. Chemistry of Intercalation Compounds: Metal Guests in Chalcogenide Hosts. *Prog. Solid St. Chem.* **1978**, *12*, 41−99.

(4) Goodenough, J. B.; Mizushima, K.; Takeda, T. Solid-Solution Oxides for Storage-Battery Electrodes. *Jpn. J. Appl. Phys.* **1980**, *19*, 305−313.

(5) Wang, Y.; Jiang, J.; Dahn, J. R. The Reactivity of Delithiated $Li(Ni_{1/3}Co_{1/3}Mn_{1/3})O_2$, $Li(Ni_{0.8}Co_{0.15}Al_{0.05})O_2$ or $LiCoO_2$ with Non-Aqueous Electrolyte. *Electrochem. Commun.* **2007**, *9*, 2534−2540.

(6) Van Bommel, A.; Dahn, J. R. Synthesis of Spherical and Dense Particles of the Pure Hydroxide Phase $Ni_{1/3}Mn_{1/3}Co_{1/3}(OH)_2$. *J. Electrochem. Soc.* **2009**, *156*, A362−A365.

(7) Kim, J.; Lee, H.; Cha, H.; Yoon, M.; Park, M.; Cho, J. Prospect and Reality of Ni-Rich Cathode for Commercialization. *Adv. Energy Mater.* **2018**, *8*, 1702028.

(8) Li, W.; Erickson, E. M.; Manthiram, A. High-Nickel Layered Oxide Cathodes for Lithium-Based Automotive Batteries. *Nat. Energy* **2020**, *5*, 26−34.

(9) Ito, A.; Li, D.; Sato, Y.; Arao, M.; Watanabe, M.; Hatano, M.; Horie, H.; Ohsawa, Y. Cyclic Deterioration and its Improvement for Li-Rich Layered Cathode Material $Li[Ni_{0.17}Li_{0.2}Co_{0.07}Mn_{0.56}]O_2$. *J. Power Sources* **2010**, *195*, 567−573.

(10) Rozier, P.; Tarascon, J. M. Review—Li-Rich Layered Oxide Cathodes for Next-Generation Li-Ion Batteries: Chances and Challenges. *J. Electrochem. Soc.* **2015**, *162*, A2490−A2499.

(11) He, W.; Guo, W.; Wu, H.; Lin, L.; Liu, Q.; Han, X.; Xie, Q.; Liu, P.; Zheng, H.; Wang, L.; Yu, X.; Peng, D.-L. Challenges and Recent Advances in High Capacity Li-Rich Cathode Materials for High Energy Density Lithium-Ion Batteries. *Adv. Mater.* **2021**, *33*, 2005937.

(12) Thackeray, M. M.; Johnson, P. J.; De Picciotto, L. A.; Bruce, P. G.; Goodenough, J. B. Electrochemical Extraction of Lithium from $LiMn_2O_4$. *Mater. Res. Bull.* **1984**, *19*, 179−187.

(13) Zhong, Q.; Bonakdarpour, A.; Zhang, M.; Gao, Y.; Dahn, J. R. Synthesis and Electrochemistry of $LiNi_xMn_{2-x}O_4$. *J. Electrochem. Soc.* **1997**, *144*, 205−213.

(14) Amine, K.; Tukamoto, H.; Yasuda, H.; Fujita, Y. Preparation and Electrochemical Investigation of $LiMn_{2-x}Me_xO_4$ (Me: Ni, Fe, and $x =$ 0.5, 1) Cathode Materials for Secondary Lithium Batteries. *J. Power Sources* **1997**, *68*, 604−608.

(15) Huang, Y.; Dong, Y.; Li, S.; Lee, J.; Wang, C.; Zhu, Z.; Xue, W.; Li, Y.; Li, J. Lithium Manganese Spinel Cathodes for Lithium-Ion Batteries. *Adv. Energy Mater.* **2021**, *11*, 2000997.

(16) Padhi, A. K.; Nanjundaswamy, K. S.; Goodenough, J. B. Phospo-Olivines as Positive-Electrode Materials for Rechargeable Lithium Batteries. *J. Electrochem. Soc.* **1997**, *144*, 1188−1194.

(17) Huang, H.; Yin, S.-C.; Nazar, L. F. Approaching Theoretical Capacity of $LiFePO_4$ at Room Temperature at High Rates. *Electrochem. Solid-State Lett.* **2001**, *4*, A170−A172.

(18) Chung, S.-Y.; Bloking, J. T.; Chiang, Y.-M. Electronically Conductive Phospho-Olivines as Lithium Storage Electrodes. *Nat. Mater.* **2002**, *1*, 123−128.

(19) Lee, J.; Urban, A.; Li, X.; Su, D.; Hautier, G.; Ceder, G. Unlocking the Potential of Cation-Disordered Oxides for Rechargeable Lithium Batteries. *Science* **2014**, *343*, 519−522.

(20) Clement, R. J.; Lun, Z.; Ceder, G. Cation-Disordered Rocksalt Transition Metal Oxides and Oxyfluorides for High Energy Lithium-Ion Cathodes. *Energy Environ. Sci.* **2020**, *13*, 345−373.

(21) Rougier, A.; Gravereau, P.; Delmas, C. Optimization of the Composition of the $Li_{1-z}Ni_{1+z}O_2$ Electrode Materials: Structural, Magnetic, and Electrochemical Studies. *J. Electrochem. Soc.* **1996**, *143*, 1168−1175.

(22) Kang, K.; Meng, Y. S.; Breger, J.; Grey, C. R.; Ceder, G. Electrode with High Power and High Capacity for Rechargeable Lithium Batteries. *Science* **2006**, *311*, 977−980.

(23) Lee, W.; Muhammad, S.; Kim, T.; Kim, H.; Lee, E.; Jeong, M.; Son, S.; Ryou, J.-H.; Yoon, W.-S. New Insight into Ni-Rich Layered Structure for Next-Generation Li Rechargeable Batteries. *Adv. Energy Mater.* **2018**, *8*, 1701788.

(24) Zhou, H.; Xin, F.; Pei, B.; Whittingham, M. S. What Limits the Capacity of Layered Oxide Cathodes in Lithium Batteries? *ACS Energy Lett.* **2019**, *4*, 1902−1906.

(25) Kasnatscheew, J.; Evertz, M.; Streipert, B.; Wagner, R.; Klopsch, R.; Vortmann, B.; Hahn, H.; Nowak, S.; Amereller, M.; Gentschev, A.-C.; et al. The Truth about the 1st Cycle Coulombic Efficiency of $LiNi_{1/3}Co_{1/3}Mn_{1/3}O_2$ (NCM) Cathodes. *Phys. Chem. Chem. Phys.* **2016**, *18*, 3956−3965.

(26) Baba, Y.; Okada, S.; Yamaki, J.-I. Thermal Stability of Li_xCoO_2 Cathode for Lithium Ion Battery. *Solid State Ionics* **2002**, *148*, 311−316.

(27) Bak, S.-M.; Hu, E.; Zhou, Y.; Yu, X.; Senanayake, S. D.; Cho, S.-J.; Kim, K.-B.; Chung, K. Y.; Yang, X.-Q.; Nam, K.-W. Structural Changes and Thermal Stability of Charged $LiNi_xMn_yCo_zO_2$ Cathode Materials

Studied by Combined In Situ Time-Resolved XRD and Mass Spectroscopy. *ACS Appl. Mater. Interfaces* **2014**, *6*, 22594−22601.

(28) Armstrong, A. R.; Holzapfel, M.; Novak, P.; Johnson, C. S.; Kang, S.-H.; Thackeray, M. M.; Bruce, P. G. Demonstrating Oxygen Loss and Associated Structural Reorganization in the Lithium Battery Cathode Li[Ni$_{0.2}$Li$_{0.2}$Mn$_{0.6}$]O$_2$. *J. Am. Chem. Soc.* **2006**, *128*, 8694−8698.

(29) Tran, N.; Croguennec, L.; Menetrier, M.; Weill, F.; Biensan, Ph.; Jordy, C.; Delmas, C. Mechanisms Associated with the "Plateau" Observed at High Voltage for the Overlithiated Li$_{1.12}$(Ni$_{0.425}$Mn$_{0.425}$Co$_{0.15}$)$_{0.88}$O$_2$ System. *Chem. Mater.* **2008**, *20*, 4815−4825.

(30) Zou, L.; Zhao, W.; Jia, H.; Zheng, J.; Li, L.; Abraham, D. P.; Chen, G.; Croy, J. R.; Zhang, J.-G.; Wang, C. The Role of Secondary Particle Structures in Surface Phase Transitions of Ni-Rich Cathodes. *Chem. Mater.* **2020**, *32*, 2884−2892.

(31) Ryu, H.-H.; Park, G.-T.; Yoon, C. S.; Sun, Y.-K. Microstructural Degradation of Ni-Rich Li[Ni$_x$Co$_y$Mn$_{1-x-y}$]O$_2$ Cathodes during Accelerated Calendar Aging. *Small* **2018**, *14*, 1803179.

(32) Liu, T.; Yu, L.; Liu, J.; Lu, J.; Bi, X.; Dai, A.; Li, M.; Li, M.; Hu, Z.; Ma, L.; et al. Understanding Co Roles towards Developing Co-Free Ni-Rich Cathodes for Rechargeable Batteries. *Nat. Energy* **2021**, *6*, 277−286.

(33) Liu, T.; Yu, L.; Lu, J.; Zhou, T.; Huang, X.; Cai, Z.; Dai, A.; Gim, J.; Ren, Y.; Xiao, X.; et al. Rational Design of Mechanically Robust Ni-Rich Cathode Materials via Concentration Gradient Strategy. *Nat. Commun.* **2021**, *12*, 6024.

(34) Mott, N. F. The Basis of the Electron Theory of Metals, with Special Reference to the Transition Metals. *Proc. Phys. Soc. A* **1949**, *62*, 416−422.

(35) Zhao, J.; Zhang, W.; Huq, A.; Misture, S. T.; Zhang, B.; Guo, S.; Wu, L.; Zhu, Y.; Chen, Z.; Amine, K.; et al. In Situ Probing and Synthetic Control of Cationic Ordering in Ni-Rich Layered Oxide Cathodes. *Adv. Energy Mater.* **2017**, *7*, 1601266.

(36) Wang, D.; Kou, R.; Ren, Y.; Sun, C.-J.; Zhao, H.; Zhang, M.-J.; Li, Y.; Huq, A.; Ko, J. Y. P.; Pan, F.; et al. Synthetic Control of Kinetic Reaction Pathway and Cationic Ordering in High-Ni Layered Oxide Cathodes. *Adv. Mater.* **2017**, *29*, 1606715.

(37) Manthiram, A. A Reflection on Lithium-Ion Battery Cathode Chemistry. *Nat. Commun.* **2020**, *11*, 1550.

(38) Liang, J.; Wu, D.; Hu, M.; Tian, Y.; Wei, J.; Zhou, Z. Could Li/Ni Disorder be Utilized Positively? Combined Experimental and Computational Investigation on Pillar Effect of Ni at Li Sites on LiCoO$_2$ at High Voltages. *Electrochem. Acta* **2014**, *146*, 784−791.

(39) Yoon, M.; Dong, Y.; Yoo, Y.; Myeong, S.; Hwang, J.; Kim, J.; Choi, S.-H.; Sung, J.; Kang, S. J.; Li, J.; Cho, J. Unveiling Nickel Chemistry in Stabilizing High-Voltage Cobalt-Rich Cathodes for Lithium-Ion Batteries. *Adv. Funct. Mater.* **2020**, *30*, 1907903.

(40) Liu, W.; Oh, P.; Liu, X.; Lee, M.-J.; Cho, W.; Chae, S.; Kim, Y.; Cho, J. Nickel-Rich Layered Lithium Transition-Metal Oxide for High-Energy Lithium-Ion Batteries. *Angew. Chem., Int. Ed.* **2015**, *54*, 4440−4457.

(41) Ryu, H.-H.; Park, K.-J.; Yoon, C. S.; Sun, Y.-K. Capacity Fading of Ni-Rich Li[Ni$_x$Co$_y$Mn$_{1-x-y}$]O$_2$ ($0.6 \leq x \leq 0.95$) Cathodes for High-Energy-Density Lithium-Ion Batteries: Bulk or Surface Degradation? *Chem. Mater.* **2018**, *30*, 1155−1163.

(42) Sun, H.-H.; Manthiram, A. Impact of Microcrack Generation and Surface Degradation on a Nickel-Rich Layered Li[Ni$_{0.9}$Co$_{0.05}$Mn$_{0.05}$]O$_2$ Cathode for Lithium-Ion Batteries. *Chem. Mater.* **2017**, *29*, 8486−8493.

(43) Seong, W. M.; Yoon, K.; Lee, M. H.; Jung, S.-K.; Kang, K. Unveiling the Intrinsic Cycle Reversibility of a LiCoO$_2$ Electrode at 4.8-V Cutoff Voltage through Subtractive Surface Modification for Lithium-Ion Batteries. *Nano Lett.* **2019**, *19*, 29−37.

(44) Zhu, Z.; Yu, D.; Shi, Z.; Gao, R.; Xiao, X.; Waluyo, I.; Ge, M.; Dong, Y.; Xue, W.; Xu, G.; et al. Gradient-Morph LiCoO$_2$ Single Crystals with Stabilized Energy Density above 3400 W h L^{-1}. *Energy Environ. Sci.* **2020**, *13*, 1865−1878.

(45) Zhu, Z.; Wang, H.; Li, Y.; Gao, R.; Xiao, X.; Yu, Q.; Wang, C.; Waluyo, I.; Ding, J.; Hunt, A.; Li, J. A Surface Se-Substituted LiCo[O$_{2-\delta}$Se$_\delta$] Cathode with Ultrastable High-Voltage Cycling in Pouch Full-Cells. *Adv. Mater.* **2020**, *32*, 2005182.

(46) Hu, E.; Yu, X.; Lin, R.; Bi, X.; Lu, J.; Bak, S.; Nam, K.-W.; Xin, H. L.; Jaye, C.; Fischer, D. A.; et al. Evolution of Redox Couples in Li- and Mn-Rich Cathode Materials and Mitigation of Voltage Fade by Reducing Oxygen Release. *Nat. Energy* **2018**, *3*, 690−698.

(47) Yan, P.; Nie, A.; Zheng, J.; Zhou, Y.; Lu, D.; Zhang, X.; Xi, R.; Belharouak, I.; Zu, X.; Xiao, J.; et al. Evolution of Lattice Structure and Chemical Composition of the Surface Reconstruction Layer in Li$_{1.2}$Ni$_{0.2}$Mn$_{0.6}$O$_2$ Cathode Material for Lithium Ion Batteries. *Nano Lett.* **2015**, *15*, 514−522.

(48) Gu, M.; Belharouak, I.; Zheng, J.; Wu, H.; Xiao, J.; Genc, A.; Amine, K.; Thevuthasan, S.; Baer, D. R.; Zhang, J.-G.; et al. Formation of the Spinel Phase in the Layered Composite Cathode Used in Li-Ion Batteries. *ACS Nano* **2013**, *7*, 760−767.

(49) Oh, P.; Myeong, S.; Cho, W.; Lee, M.-J.; Ko, M.; Jeong, H. Y.; Cho, J. Superior Long-Term Energy Retention and Volumetric Energy Density for Li-Rich Cathode Materials. *Nano Lett.* **2014**, *14*, 5965−5972.

(50) Goodenough, J. B.; Kim, Y. Challenges for Rechargeable Li Batteries. *Chem. Mater.* **2010**, *22*, 587−603.

(51) Goodenough, J. B.; Park, K.-S. The Li-Ion Rechargeable Battery: A Perspective. *J. Am. Chem. Soc.* **2013**, *135*, 1167−1176.

(52) Zhang, J.-N.; Li, Q.; Ouyang, C.; Yu, X.; Ge, M.; Huang, X.; Hu, E.; Ma, C.; Li, S.; Xiao, R.; et al. Trace Doping of Multiple Elements enables Stable Battery Cycling of LiCoO$_2$ at 4.6 V. *Nat. Energy* **2019**, *4*, 594−603.

(53) Qian, J.; Liu, L.; Yang, J.; Li, S.; Wang, X.; Zhuang, H. L.; Lu, Y. Electrochemical Surface Passivation of LiCoO$_2$ Particles at Ultrahigh Voltage and its Applications in Lithium-based Batteries. *Nat. Commun.* **2018**, *9*, 4918.

(54) Lyu, Y.; Wu, X.; Wang, K.; Feng, Z.; Cheng, T.; Liu, Y.; Wang, M.; Chen, R.; Xu, L.; Zhou, J.; et al. An Overview on the Advances of LiCoO$_2$ Cathodes for Lithium-Ion Batteries. *Adv. Energy Mater.* **2021**, *11*, 2000982.

(55) Armstrong, A. R.; Bruce, P. G. Synthesis of Layered LiMnO$_2$ as an Electrode for Rechargeable Lithium Batteries. *Nature* **1996**, *381*, 499−500.

(56) Lee, Y. S.; Sun, Y. K.; Ota, S.; Miyashita, T.; Yoshio, M. Preparation and Characterization of Nano-Crystalline LiNi$_{0.5}$Mn$_{1.5}$O$_4$ for 5 V Cathode Material by Composite Carbonate Process. *Electrochem. Commun.* **2002**, *4*, 989−994.

(57) Okada, S.; Sawa, S.; Egashira, M.; Yamaki, J.-I.; Tabuchi, M.; Kageyama, H.; Konishi, T.; Yoshino, A. Cathode Properties of Phospho-Olivine LiMPO$_4$ for Lithium Secondary Batteries. *J. Power Sources* **2001**, *97*, 430−432.

(58) Li, G.; Azuma, H.; Tohda, M. LiMnPO$_4$ as the Cathode for Lithium Batteries. *Electrochem. Solid-State Lett.* **2002**, *5*, A135−A137.

(59) Wolfenstine, J.; Allen, J. LiNiPO$_4$-LiCoPO$_4$ Solid Solutions as Cathodes. *J. Power Sources* **2004**, *136*, 150−153.

(60) Mauger, A.; Julien, C. M.; Armand, M.; Goodenough, J. B.; Zaghib, K. Li(Ni,Co)PO$_4$ as Cathode Materials for Lithium Batteries: Will the Dream come true? *Curr. Opin. Electrochem.* **2017**, *6*, 63−69.

(61) Niu, J.; Kushima, A.; Qian, X.; Qi, L.; Xiang, K.; Chiang, Y.-M.; Li, J. In Situ Observation of Random Solid Solution Zone in LiFePO$_4$ Electrode. *Nano Lett.* **2014**, *14*, 4005−4010.

(62) Liu, H.; Strobridge, F. C.; Borkiewicz, O. J.; Wiaderek, K. M.; Chapman, K. W.; Chupas, P. J.; Grey, C. P. Capturing Metastable Structures during High-Rate Cycling of LiFePO$_4$ Nanoparticle Electrodes. *Science* **2014**, *344*, 1252817.

(63) Lim, J.; Li, Y.; Alsem, D. H.; So, H.; Lee, S. C.; Bai, P.; Cogswell, D. A.; Liu, X.; Jin, N.; Yu, Y.-S.; et al. *Origin and Hysteresis of Lithium Compositional Spatiodynamics within Battery Primary Particles.* **2016**, *353*, 566−571.

(64) Takahashi, M.; Ohtsuka, H.; Akuto, K.; Sakurai, Y. Confirmation of Long-term Cyclability and High Thermal Stability of LiFePO$_4$ in Prismatic Lithium-Ion Cells. *J. Electrochem. Soc.* **2005**, *152*, A899−A904.

(65) Takahashi, M.; Yobishima, S.; Takei, K.; Sakurai, Y. Reaction Behavior of LiFePO$_4$ as a Cathode Material for Rechargeable Lithium Batteries. *Solid State Ionics* **2002**, *148*, 283−289.

(66) Stroukoff, K. R.; Manthiram, A. Thermal Stability of Spinel Li$_{1.1}$Mn$_{1.9-y}$M$_y$O$_{4-z}$F$_z$ (M = Ni, Al, and Li, 0 ≤ y ≤ 0.3, and 0 ≤ z ≤ 0.2) Cathodes for Lithium-Ion Batteries. *J. Mater. Chem.* **2011**, *21*, 10165−10170.

(67) Kim, J.-H.; Park, K.-J.; Kim, S. J.; Yoon, C. S.; Sun, Y.-K. A Method of Increasing the Energy Density of Layered Ni-Rich Li[Ni$_{1-2x}$Co$_x$Mn$_x$]O$_2$ Cathodes (x = 0.05, 0.1, 0.2). *J. Mater. Chem. A* **2019**, *7*, 2694−2701.

(68) Noh, H.-J.; Youn, S.; Yoon, C. S.; Sun, Y.-K. Comparison of the Structural and Electrochemical Properties of Layered Li[Ni$_x$Co$_y$Mn$_z$]-O$_2$ (x = 1/3, 0.5, 0.6, 0.7, 0.8 and 0.85) Cathode Material for Lithium-Ion Batteries. *J. Power Sources* **2013**, *233* (233), 121−130.

(69) Fan, X.; Wang, C. High-Voltage Liquid Electrolytes for Li Batteries: Progress and Perspectives. *Chem. Soc. Rev.* **2021**, *50*, 10486−10566.

(70) Suo, L.; Xue, W.; Gobet, M.; Greenbaum, S. G.; Wang, C.; Chen, Y.; Yang, W.; Li, Y.; Li, J. Fluorine-Donating Electrolytes Enable Highly Reversible 5-V-Class Li Metal Batteries. *Proc. Natl. Acad. Sci. U.S.A.* **2018**, *115*, 1156−1161.

(71) Seo, D.-H.; Lee, J.; Urban, A.; Malik, R.; Kang, S. Y.; Ceder, G. The Structural and Chemical Origin of the Oxygen Redox Activity in Layered and Cation-Disordered Li-Excess Cathode Materials. *Nat. Chem.* **2016**, *8*, 692−697.

(72) Luo, K.; Roberts, M. R.; Hao, R.; Guerrini, N.; Pickup, D. M.; Liu, Y.-S.; Edstrom, K.; Guo, J.; Chadwick, A. V.; Duda, L. C.; Bruce, P. G. Charge-Compensation in 3d-Transition-Metal-Oxide Intercalation Cathodes through the Generation of Localized Electron Holes on Oxygen. *Nat. Chem.* **2016**, *8*, 684−691.

(73) Luo, K.; Roberts, M. R.; Hao, R.; Guerrini, N.; Tapia-Ruiz, N.; Hao, R.; Massel, F.; Pickup, D. M.; Ramos, S.; Liu, Y.-S.; et al. Anion Redox Chemistry in the Cobalt Free 3d Transition Metal Oxide Intercalation Electrode Li[Li$_{0.2}$Ni$_{0.2}$Mn$_{0.6}$]O$_2$. *J. Am. Chem. Soc.* **2016**, *138*, 11211−11218.

(74) Lun, Z.; Ouyang, B.; Kitchaev, D. A.; Clement, R. J.; Papp, J. K.; Balasubramanian, M.; Tian, Y.; Lei, T.; Shi, T.; McCloskey, B. D.; et al. Improved Cycling Performance of Li-Excess Cation-Disordered Cathode Materials upon Fluorine Substitution. *Adv. Energy Mater.* **2019**, *9*, 1802959.

(75) Yabuuchi, N.; Takeuchi, M.; Nakayama, M.; Shiiba, H.; Ogawa, M.; Nakayama, K.; Ohta, T.; Endo, D.; Ozaki, T.; Inamasu, T.; et al. High-Capacity Electrode Materials for Rechargeable Lithium Batteries: Li$_3$NbO$_4$-based System with Cation-Disordered Rocksalt Structure. *Proc. Natl. Acad. Sci. U.S.A.* **2015**, *112*, 7650−7655.

(76) Lee, J.; Wang, C.; Malik, R.; Dong, Y.; Huang, Y.; Seo, D.-H.; Li, J. Determining the Criticality of Li-Excess for Disordered-Rocksalt Li-Ion Battery Cathodes. *Adv. Energy Mater.* **2021**, *11*, 2100204.

(77) Li, S.; Sun, X.; Liu, Y.; Liu, G.; Xue, W.; Waluyo, I.; Zhu, Z.; Zhu, Y.; Dong, Y.; Huang, Y.; Li, J. Thermally Aged Li-Mn-O Cathode with Stabilized Hybrid Cation and Anion Redox. *Nano Lett.* **2021**, *21*, 4176−4184.

(78) Dong, Y.; Huang, Y.; Ding, D.; Wu, W.; Yao, X.; Li, J. Chemical and Structural Origin of Hole States in Yttria-Stabilized Zirconia. *Acta Mater.* **2021**, *203*, 116487.

(79) Yoon, M.; Dong, Y.; Hwang, J.; Sung, J.; Cha, H.; Ahn, K.; Huang, Y.; Kang, S. J.; Li, J.; Cho, J. Reactive Boride Infusion Stabilizes Ni-Rich Cathodes for Lithium-Ion Batteries. *Nat. Energy* **2021**, *6*, 362−371.

(80) Assat, G.; Foix, D.; Delacourt, C.; Iadecola, A.; Dedryvere, R.; Tarascon, J.-M. Fundamental Interplay between Anionic/Cationic Redox Governing the Kinetics and Thermodynamics of Lithium-Rich Cathodes. *Nat. Common.* **2017**, *8*, 2219.

(81) Assat, G.; Tarascon, J.-M. Fundamental Understanding of Practical Challenges of Anionic Redox Activity in Li-Ion Batteries. *Nat. Energy* **2018**, *3*, 373−386.

(82) Zhu, Z.; Yu, D.; Yang, Y.; Su, C.; Huang, Y.; Dong, Y.; Waluyo, I.; Wang, B.; Hunt, A.; Yao, X.; et al. Gradient Li-Rich Oxide Cathode Particles Immunized against Oxygen Release by a Molten Salt Treatment. *Nat. Energy* **2019**, *4*, 1049−1058.

(83) Zhang, M.; Kitchaev, D. A.; Lebens-Higgins, Z.; Vinckeviciute, J.; Zuba, M.; Reeves, P. J.; Grey, C. P.; Whittingham, M. S.; Piper, L. F. J.; Van der Ven, A.; Meng, Y. S. Pushing the Limit of 3d Transition Metal-based Layered Oxides that Use Both Cation and Anion Redox for Energy Storage. *Nat. Rev. Mater.* **2022**, *7*, 522−540.

(84) McCalla, E.; Abakumov, A. M.; Saubanere, M.; Foix, D.; Berg, E. J.; Rousse, G.; Doublet, M.-L.; Gonbeau, D.; Novak, P.; Van Tendeloo, G.; et al. Visualization of O-O Peroxo-Like Dimers in High-Capacity Layered Oxides for Li-Ion Batteries. *Science* **2015**, *350*, 1516−1521.

(85) Chen, H.; Islam, M. S. Lithium Extraction Mechanism in Li-Rich Li$_2$MnO$_3$ Involving Oxygen Hole Formation and Dimerization. *Chem. Mater.* **2016**, *28*, 6656−6663.

(86) Ning, F.; Li, B.; Song, J.; Zuo, Y.; Shang, H.; Zhao, Z.; Yu, Z.; Chu, W.; Zhang, K.; Feng, G.; et al. Inhibition of Oxygen Dimerization by Local Symmetry Tuning in Li-Rich Layered Oxides for Improved Stability. *Nat. Commun.* **2020**, *11*, 4973.

(87) Kitchaev, D. A.; Vinckeviciute, J.; Van der Ven, A. Delocalized Metal-Oxygen π-Redox is the Origin of Anomalous Nonhysteretic Capacity in Li-Ion and Na-Ion Cathode Materials. *J. Am. Chem. Soc.* **2021**, *143*, 1908−1916.

(88) House, R. A.; Rees, G. J.; Perez-Osorio, M. A.; Marie, J.-J.; Boivin, E.; Robertson, A. W.; Nag, A.; Garcia-Fernandez, M.; Zhou, K.-J.; Bruce, P. G. First-Cycle Voltage Hysteresis in Li-Rich 3d Cathodes Associated with Molecular O$_2$ trapped in the Bulk. *Nat. Energy* **2020**, *5*, 777−785.

(89) House, R. A.; Maitra, U.; Perez-Osorio, M. A.; Lozano, J. G.; Jin, L.; Somerville, J. W.; Duda, L. C.; Nag, A.; Walters, A.; Zhou, K.-J.; et al. Superstructure Control of First-Cycle Voltage Hysteresis in Oxygen-Redox Cathodes. *Nature* **2020**, *577*, 502−508.

(90) House, R. A.; Marie, J.-J.; Perez-Osorio, M. A.; Rees, G. J.; Boivin, E.; Bruce, P. G. The Role of O$_2$ in O-Redox Cathodes for Li-Ion Batteries. *Nat. Energy* **2021**, *6*, 781−789.

(91) Zhang, S.; Zhao, K.; Zhu, T.; Li, J. Electrochemomechanical Degradation of High-Capacity Battery Electrode Materials. *Prog. Mater. Sci.* **2017**, *89*, 479−521.

(92) Sharifi-Asl, S.; Lu, J.; Amine, K.; Shahbazian-Yassar, R. Oxygen Release Degradation in Li-Ion Battery Cathode Materials: Mechanisms and Mitigation Approaches. *Adv. Energy Mater.* **2019**, *9*, 1900551.

(93) Zhang, H.; Liu, H.; Piper, L. F. J.; Whittingham, M. S.; Zhou, G. Oxygen loss in Layered Oxide Cathodes for Li-Ion Batteries: Mechanisms, Effects, and Mitigation. *Chem. Rev.* **2022**, *122*, 5641−5681.

(94) Gallus, D. R.; Wagner, R.; Wiemers-Meyer, S.; Winter, M.; Cekic-Laskovic, I. New Insights into the Structure-Property Relationship of High-Voltage Electrolyte Components for Lithium-Ion Batteries Using the pK$_a$ Value. *Electrochem. Acta* **2015**, *184*, 410−416.

(95) Li, J.; Li, W.; You, Y.; Manthiram, A. Extending the Service Life of High-Ni Layered Oxides by Tuning the Electrode-Electrolyte Interphase. *Adv. Energy Mater.* **2018**, *8*, 1801957.

(96) Lee, S.; Li, W.; Dolocan, A.; Celio, H.; Park, H.; Warner, J. H.; Manthiram, A. In-Depth Analysis of the Degradation Mechanisms of High-Nickel, Low/No-Cobalt Layered Oxide Cathodes for Lithium-Ion Batteries. *Adv. Energy Mater.* **2021**, *11*, 2100858.

(97) Zhang, J.-N.; Li, Q.; Wang, Y.; Zheng, J.; Yu, X.; Li, H. Dynamic Evolution of Cathode Electrolyte Interphase (CEI) on High Voltage LiCoO$_2$ Cathode and its Interaction with Li Anode. *Energy Storage Mater.* **2018**, *14*, 1−7.

(98) Zhang, Z.; Yang, J.; Huang, W.; Wang, H.; Zhou, W.; Li, Y.; Li, Y.; Xu, J.; Huang, W.; Chiu, W.; Cui, Y. Cathode-Electrolyte Interphase in Lithium Batteries Revealed by Cryogenic Electron Microscopy. *Matter* **2021**, *4*, 302−312.

(99) Peled, E. The Electrochemical Behavior of Alkali and Alkaline Earth Metals in Nonaqueous Battery Systems—The Solid Electrolyte Interphase Model. *J. Electrochem. Soc.* **1979**, *126*, 2047−2051.

(100) Peled, E.; Menkin, S. Review—SEI: Past, Present and Future. *J. Electrochem. Soc.* **2017**, *164*, A1703−A1719.

(101) Han, B.; Zou, Y.; Xu, G.; Hu, S.; Kang, Y.; Qian, Y.; Wu, J.; Ma, X.; Yao, J.; Li, T.; et al. Additive Stabilization of SEI on Graphite Observed Using Cryo-Electron Microscopy. *Energy Environ. Sci.* **2021**, *14*, 4882.

(102) Han, B.; Li, X.; Wang, Q.; Zou, Y.; Xu, G.; Cheng, Y.; Zhang, Z.; Zhao, Y.; Deng, Y.; Li, J.; Gu, M. Cryo-Electron Tomography of Highly Deformable and Adherent Solid-Electrolyte Interphase Exoskeleton in Li-Metal Batteries with Ether-based Electrolyte. *Adv. Mater.* **2022**, *34*, 2108252.

(103) Fan, X.; Chen, L.; Borodin, O.; Ji, X.; Chen, J.; Hou, S.; Deng, T.; Zheng, J.; Yang, C.; Liou, S.-C.; et al. Non-Flammable Electrolyte Enables Li-Metal Batteries with Aggressive Cathode Chemistries. *Nat. Nanotechnol.* **2018**, *13*, 715−722.

(104) Martha, S. K.; Nanda, J.; Kim, Y.; Unocic, R. R.; Pannala, S.; Dudney, N. J. Solid Electrolyte Coated High Voltage Layered-Layered Lithium-Rich Composite Cathode: $Li_{1.2}Mn_{0.525}Ni_{0.175}Co_{0.1}O_2$. *J. Mater. Chem. A* **2013**, *1*, 5587−5595.

(105) Cho, J.; Kim, Y. J.; Park, B. Novel $LiCoO_2$ Cathode Material with Al_2O_3 Coating for a Li Ion Cell. *Chem. Mater.* **2000**, *12*, 3788−3791.

(106) Zheng, J.; Gu, M.; Xiao, J.; Polzin, B. J.; Yan, P.; Chen, X.; Wang, C.; Zhang, J.-G. Functioning Mechanism of AlF_3 Coating on the Li- and Mn-Rich Cathode Materials. *Chem. Mater.* **2014**, *26*, 6320−6327.

(107) Zhu, Z.; Gao, R.; Waluyo, I.; Dong, Y.; Hunt, A.; Lee, J.; Li, J. Stabilized Co-Free Li-Rich Oxide Cathode Particles with an Artificial Surface Prereconstruction. *Adv. Energy Mater.* **2020**, *10*, 2001120.

(108) Zhan, C.; Wu, T.; Lu, J.; Amine, K. Dissolution, Migration, and Deposition of Transition Metal Ions in Li-Ion Batteries Exemplified by Mn-based Cathodes - A Critical Review. *Energy Environ. Sci.* **2018**, *11*, 243−257.

(109) Li, W.; Liu, X.; Celio, H.; Smith, P.; Dolocan, A.; Chi, M.; Manthiram, A. Mn versus Al in Layered Oxide Cathodes in Lithium-Ion Batteries: A Comprehensive Evaluation on Long-Term Cyclability. *Adv. Energy Mater.* **2018**, *8*, 1703154.

(110) Li, W.; Liu, X.; Xie, Q.; You, Y.; Chi, M.; Manthiram, A. Long-Term Cyclability of NCM-811 at High Voltages in Lithium-Ion Batteries: An In-Depth Diagnostic Study. *Chem. Mater.* **2020**, *32*, 7796−7804.

(111) Joshi, T.; Eom, K.; Yushin, G.; Fuller, T. F. Effects of Dissolved Transition Metals on the Electrochemical Performance and SEI Growth in Lithium-Ion Batteries. *J. Electrochem. Soc.* **2014**, *161*, A1915−A1921.

(112) Cho, I. H.; Kim, S.-S.; Shin, S. C.; Choi, N.-S. Effect of SEI on Capacity Losses of Spinel Lithium Manganese Oxide/Graphite Batteries Stored at 60 °C. *Electrochem. Solid-State Lett.* **2010**, *13*, A168−A172.

(113) Friedrich, F.; Strehle, B.; Freiberg, A. T. S.; Kleiner, K.; Day, S. J.; Erk, C.; Piana, M.; Gasteiger, H. A. Capacity Fading mechanisms of NCM-811 Cathodes in Lithium-Ion Batteries Studied by X-Ray Diffraction and Other Diagnostics. *J. Electrochem. Soc.* **2019**, *166*, A3760−A3774.

(114) Xue, W.; Huang, M.; Li, Y.; Zhu, Y. G.; Gao, R.; Xiao, X.; Zhang, W.; Li, S.; Xu, G.; Yu, Y.; et al. Ultra-High-Voltage Ni-Rich Layered Cathodes in Practical Li Metal Batteries Enabled by a Sulfonamide-based Electrolyte. *Nat. Energy* **2021**, *6*, 495−505.

(115) Li, W.; Dolocan, A.; Li, J.; Xie, Q.; Manthiram, A. Ethylene Carbonate-Free Electrolytes for High-Nickel Layered Oxide Cathodes in Lithium-Ion Batteries. *Adv. Energy Mater.* **2019**, *9*, 1901152.

(116) Yan, P.; Zheng, J.; Liu, J.; Wang, B.; Cheng, X.; Zhang, Y.; Sun, X.; Wang, C.; Zhang, J.-G. Tailoring Grain Boundary Structures and Chemistry of Ni-Rich Layered Cathodes for Enhanced Cycle Stability of Lithium-Ion Batteries. *Nat. Energy* **2018**, *3*, 600−605.

(117) Kim, J.; Lee, J.; Ma, H.; Jeong, H. Y.; Cha, H.; Lee, H.; Yoo, Y.; Park, M.; Cho, J. Controllable Solid Electrolyte Interphase in Nickel-Rich Cathodes by an Electrochemical Rearrangement for Stable Lithium-Ion Batteries. *Adv. Mater.* **2018**, *30*, 1704309.

(118) Sieradzki, K.; Newman, R. C. Stress-Corrosion Cracking. *J. Phys. Chem. Solid* **1987**, *48*, 1101−1113.

(119) Yan, P.; Zheng, J.; Tang, Z.-K.; Devaraj, A.; Chen, G.; Amine, K.; Zhang, J.-G.; Liu, L.-M.; Wang, C. Injection of Oxygen Vacancies in the Bulk Lattice of Layered Cathodes. *Nat. Nanotechnol.* **2019**, *14*, 602−608.

(120) Hu, W.; Wang, H.; Luo, W.; Xu, B.; Ouyang, C. Formation and Thermodynamic Stability of Oxygen Vacancies in Typical Cathode Materials for Li-Ion Batteries: Density Functional Theory Study. *Solid State Ionics* **2020**, *347*, 115257.

(121) Kong, F.; Liang, C.; Wang, L.; Zheng, Y.; Perananthan, S.; Longo, R. C.; Ferraris, J. P.; Kim, M.; Cho, K. Kinetic Stability of Bulk $LiNiO_2$ and Surface Degradation by Oxygen Evolution in $LiNiO_2$-based Cathode Materials. *Adv. Energy Mater.* **2019**, *9*, 1802586.

(122) Jiang, Z.; Li, J.; Yang, Y.; Mu, L.; Wei, C.; Yu, X.; Pianetta, P.; Zhao, K.; Cloetens, P.; Lin, F.; Liu, Y. Machine-Learning-Revealed Statistics of the Particle-Carbon/Binder Detachment in Lithium-Ion Battery Cathodes. *Nat. Commun.* **2020**, *11*, 2310.

(123) Gent, W. E.; Lim, K.; Liang, Y.; Li, Q.; Barnes, T.; Ahn, S.-J.; Stone, K. H.; McIntire, M.; Hong, J.; Song, J. H.; et al. Coupling between Oxygen Redox and Cation Migration Explains Unusual Electrochemistry in Lithium-Rich Layered Oxides. *Nat. Commun.* **2017**, *8*, 2091.

(124) Lin, F.; Zhao, K.; Liu, Y. Heterogeneous Reaction Activities and Statistical Characteristics of Particle Cracking in Battery Electrode. *ACS Energy Lett.* **2021**, *6*, 4065−4070.

(125) Dong, Y.; Zhang, Z.; Alvarez, A.; Chen, I. W. Potential Jumps at Transport Bottlenecks Cause Instability of Nominally Ionic Solid Electrolytes in Electrochemical Cells. *Acta Mater.* **2020**, *199*, 264−277.

(126) Dong, Y.; Chen, I. W.; Li, J. Transverse and Longitudinal Degradations in Ceramic Solid Electrolytes. *Chem. Mater.* **2022**, *34*, 5749−5765.

(127) Krauskopf, T.; Richter, F. H.; Zeier, W. G.; Janek, J. Physicochemical Concepts of the Lithium Metal Anode in Solid-State Batteries. *Chem. Rev.* **2020**, *120*, 7745−7794.

(128) Lou, S.; Liu, Q.; Zhang, F.; Liu, Q.; Yu, Z.; Mu, T.; Zhao, Y.; Borovilas, J.; Chen, Y.; Ge, M.; et al. Insights into Interfacial Effect and Local Lithium-Ion Transport in Polycrystalline Cathodes of Solid-State Batteries. *Nat. Commun.* **2020**, *11*, 5700.

(129) Mu, L.; Yuan, Q.; Tian, C.; Wei, C.; Zhang, K.; Liu, J.; Pianetta, P.; Doeff, M. M.; Liu, Y.; Lin, F. Propagation Topography of Redox Phase Transformations in Heterogeneous Layered Oxide Cathode Materials. *Nat. Commun.* **2018**, *9*, 2810.

(130) Li, Y.; El Gabaly, F. E.; Ferguson, T. R.; Smith, R. B.; Bartelt, N. C.; Sugar, J. D.; Fenton, K. R.; Cogswell, D. A.; Kilcoyne, A. L. D.; Tyliszczak, T.; et al. Current-Induced Transition from Particle-by-Particle to Concurrent Intercalation in Phase-Separating Battery Electrodes. *Nat. Mater.* **2014**, *13*, 1149−1156.

(131) Li, J.; Sharma, N.; Jiang, Z.; Yang, Y.; Monaco, F.; Xu, Z.; Hou, D.; Ratner, D.; Pianetta, P.; Cloetens, P.; et al. Dynamics of Particle Network in Composite Battery Cathode. *Science* **2022**, *376*, 517−521.

(132) Lee, E.; Persson, K. A. Structural and Chemical Evolution of the Layered Li-Excess Li_xMnO_3 as a Function of Li Content from First-Principles Calculations. *Adv. Energy Mater.* **2014**, *4*, 1400498.

(133) Kresse, G.; Joubert, D. From Ultrasoft Pseudopotentials to the Projector Augmented-Wave Method. *Phys. Rev. B* **1999**, *59*, 1758.

(134) Kresse, G.; Furthmüller, J. Efficiency of Ab-Initio Total Energy Calculations for Metals and Semiconductors Using a Plane-Wave Basis Set. *Comput. Mater. Sci.* **1996**, *6*, 15−50.

(135) Perdew, J. P.; Burke, K.; Ernzerhof, M. Generalized Gradient Approximation Made Simple. *Phys. Rev. Lett.* **1996**, *77*, 3865−3868.

(136) Dudarev, S. L.; Botton, G. A.; Savrasov, S. Y.; Humphreys, C. J.; Sutton, A. P. Electron-Energy-Loss Spectra and the Structural Stability of Nickel Oxide: an LSDA + U Study. *Phys. Rev. B* **1998**, *57*, 1505−1509.

(137) Jain, A.; Hautier, G.; Ong, S. P.; Moore, C. J.; Fischer, C. C.; Persson, K. A.; Ceder, G. Formation Enthalpies by Mixing GGA and GGA + U Calculations. *Phys. Rev. B* **2011**, *84*, 045115.

(138) Henkelman, G.; Uberuaga, B. P.; Jonsson, H. A. A Climbing Image Nudged Elastic Band Method for Finding Saddle Points and Minimum Energy Paths. *J. Chem. Phys.* **2000**, *113*, 9901−9904.

(139) Xiao, P.; Sheppard, D.; Rogal, J.; Henkelman, G. Solid-State Dimer Method for Calculating Solid-Solid Phase Transitions. *J. Chem. Phys.* **2014**, *140*, 174104.

(140) Dong, Y.; Chen, I. W.; Li, J.Hole Polaron Assisted Oxygen Ion Migration in Li$_2$MnO$_3$. *arXiv*2019, 1908.05754.

(141) Dong, Y.; Qi, L.; Alvarez, A.; Li, J.; Chen, I. W. Enhanced Mobility of Cations and Anions in the Redox State: The Polaronium Mechanism. *Acta Mater.* **2022**, *232*, 117941.

(142) Momma, K.; Izumi, F. VESTA 3 for Three-Dimensional Visualization of Crystal, Volumetric and Morphology Data. *J. Appl. Crystallogr.* **2011**, *44*, 1272−1276.

(143) Tang, W.; Sanville, E.; Henkelman, G. A Grid-based Bader Analysis Algorithm without Lattice Bias. *J. Phys.: Condens. Matter* **2009**, *21*, 084204.

(144) Lin, Q.; Guan, W.; Zhou, J.; Meng, J.; Huang, W.; Chen, T.; Gao, Q.; Wei, X.; Zeng, Y.; Li, J.; Zhang, Z. Ni-Li Anti-Site Defect Induced Intragranular Cracking in Ni-Rich Layer-Structured Cathode. *Nano Energy* **2020**, *76*, 105021.

(145) Sun, C.; Liao, X.; Xia, F.; Zhao, Y.; Zhang, L.; Mu, S.; Shi, S.; Li, Y.; Peng, H.; Van Tendeloo, G.; Zhao, K.; Wu, J. High-Voltage Cycling Induced Thermal Vulnerability in LiCoO$_2$ Cathode: Cation Loss and Oxygen Release Driven by Oxygen Vacancy Migration. *ACS Nano* **2020**, *14*, 6181−6190.

(146) Li, Y.; Li, X.; Du, C.; Sun, H.; Zhang, Y.; Liu, Q.; Yang, T.; Zhao, J.; Delmas, C.; Harris, S. J.; et al. Degradation by Kinking in Layered Cathode Materials. *ACS Energy Lett.* **2021**, *6*, 3960−3969.

(147) Singer, A.; Zhang, M.; Hy, S.; Cela, D.; Fang, C.; Wynn, T. A.; Qiu, B.; Xia, Y.; Liu, Z.; Ulvestad, A.; et al. Nucleation of Dislocations and their Dynamics in Layered Oxide Cathode Materials during Battery Charging. *Nat. Energy* **2018**, *3*, 641−647.

(148) Bi, Y.; Tao, J.; Wu, Y.; Li, L.; Xu, Y.; Hu, E.; Wu, B.; Hu, J.; Wang, C.; Zhang, J.-G.; et al. Reversible Planar Gliding and Microcracking in a Single-Crystalline Ni-Rich Cathode. *Science* **2020**, *370*, 1313−1317.

(149) Xu, R.; Sun, H.; De Vasconcelos, L. S.; Zhao, K. Mechanical and Structural Degradation of LiNi$_x$Mn$_y$Co$_z$O$_2$ Cathode in Li-Ion Batteries: An Experimental Study. *J. Electrochem. Soc.* **2017**, *164*, A3333−A3341.

(150) Li, S.; Li, Q.; Carpick, R. W.; Gumbsch, P.; Liu, X. Z.; Ding, X.; Sun, J.; Li, J. The Evolving Quality of Frictional Contact with Graphene. *Nature* **2016**, *539*, 541−545.

(151) Zou, L.; Li, J.; Liu, Z.; Wang, G.; Manthiram, A.; Wang, C. Lattice Doping Regulated Interfacial Reactions in Cathode for Enhanced Cycling Stability. *Nat. Commun.* **2019**, *10*, 3447.

(152) Lu, J.; Zhan, C.; Wu, T.; Wen, J.; Lei, Y.; Kropf, A. J.; Wu, H.; Miller, D. J.; Elam, J. W.; Sun, Y.-K.; et al. Effectively Suppressing Dissolution of Manganese from Spinel Lithium Manganate via a Nanoscale Surface-Doping Approach. *Nat. Commun.* **2014**, *5*, 5693.

(153) Bao, W.; Qian, G.; Zhao, L.; Yu, Y.; Su, L.; Cai, X.; Zhao, H.; Zuo, Y.; Zhang, Y.; Li, H.; et al. Simultaneous Enhancement of Interfacial Stability and Kinetics of Single-Crystal LiNi$_{0.6}$Mn$_{0.2}$Co$_{0.2}$O$_2$ through Optimized Surface Coating and Doping. *Nano Lett.* **2020**, *20*, 8832−8840.

(154) Sun, Y.-K.; Chen, Z.; Noh, H.-J.; Lee, D.-J.; Jung, H.-G.; Ren, Y.; Wang, S.; Yoon, C. S.; Myung, S.-T.; Amine, K. Nanostructured High-Energy Cathode Materials for Advanced Lithium Batteries. *Nat. Mater.* **2012**, *11*, 942−947.

(155) Sun, Y.-K.; Kim, D.-H.; Yoon, C. S.; Myung, S.-T.; Prakash, J.; Amine, K. A Novel Cathode Material with a Concentration-Gradient for High-Energy and Safe Lithium-Ion Batteries. *Adv. Funct. Mater.* **2010**, *20*, 485−491.

(156) Xu, Z.; Jiang, Z.; Kuai, C.; Xu, R.; Qin, C.; Zhang, Y.; Rahman, M. M.; Wei, C.; Nordlund, D.; Sun, C.-J.; et al. Charge Distribution Guided by Grain Crystallographic Orientations in Polycrystalline Battery Materials. *Nat. Commun.* **2020**, *11*, 83.

(157) Kim, U.-H.; Park, G.-T.; Son, B.-K.; Nam, G. W.; Liu, J.; Kuo, L.-Y.; Kaghazchi, P.; Yoon, C. S.; Sun, Y.-K. Heuristic Solution for Achieving Long-Term Cycle Stability for Ni-Rich Layered Cathodes at Full Depth of Discharge. *Nat. Energy* **2020**, *5*, 860−869.

(158) Cha, H.; Kim, J.; Lee, H.; Kim, N.; Hwang, J.; Sung, J.; Yoon, M.; Kim, K.; Cho, J. Boosting Reaction Homogeneity in High-Energy Lithium-Ion Battery Cathode Materials. *Adv. Mater.* **2020**, *32*, 2003040.

(159) Li, H.; Li, J.; Zaker, N.; Zhang, N.; Botton, G. A.; Dahn, J. R. Synthesis of Single Crystal LiNi$_{0.88}$Co$_{0.09}$Al$_{0.03}$O$_2$ with a Two-Step Lithiation Method. *J. Electrochem. Soc.* **2019**, *166*, A1956−A1963.

(160) Qian, G.; Zhang, Y.; Li, L.; Zhang, R.; Xu, J.; Cheng, Z.; Xie, S.; Wang, H.; Rao, Q.; He, Y.; et al. Single-Crystal Nickel-Rich Layered Oxide Battery Cathode Materials: Synthesis, Electrochemistry, and Intra-Granular Fracture. *Energy Storage Mater.* **2020**, *27*, 140−149.

(161) Hwang, J.; Myeong, S.; Lee, E.; Jang, H.; Yoon, M.; Cha, H.; Sung, J.; Kim, M. G.; Seo, D.-H.; Cho, J. Lattice-Oxygen-Stabilized Li- and Mn-Rich Cathodes with Sub-Micrometer Particles by Modifying the Excess-Li Distribution. *Adv. Mater.* **2021**, *33*, 2100352.

(162) Zhang, X.; Belharouak, I.; Li, L.; Lei, Y.; Elam, J. W.; Nie, A.; Chen, X.; Yassar, R. S.; Axelbaum, R. L. Structural and Electrochemical Study of Al$_2$O$_3$ and TiO$_2$ Coated Li$_{1.2}$Ni$_{0.13}$Mn$_{0.54}$Co$_{0.13}$O$_2$ Cathode Material Using ALD. *Adv. Energy Mater.* **2013**, *3*, 1299−1307.

(163) Li, X.; Liu, J.; Banis, M. N.; Lushington, A.; Li, R.; Cai, M.; Sun, X. Atomic Layer Deposition of Solid-State Electrolyte Coated Cathode Materials with Superior High-Voltage Cycling Behavior for Lithium Ion Battery Application. *Energy Environ. Sci.* **2014**, *7*, 768−778.

(164) Xu, G.-L.; Liu, Q.; Lau, K. K. S.; Liu, Y.; Liu, X.; Gao, H.; Zhou, X.; Zhuang, M.; Ren, Y.; Li, J.; et al. Building Ultraconformal Protective Layers on Both Secondary and Primary Particles of Layered Lithium Transition Metal Oxide Cathodes. *Nat. Energy* **2019**, *4*, 484−494.

(165) Liu, T.; Yu, L.; Lu, J.; Zhou, T.; Huang, X.; Cai, Z.; Dai, A.; Gim, J.; Ren, Y.; Xiao, X.; et al. Rational Design of Mechanically Robust Ni-Rich Cathode Materials via Concentration Gradient Strategy. *Nat. Commun.* **2021**, *12*, 6024.

(166) Sun, Y.-K.; Myung, S.-T.; Park, B.-C.; Prakash, J.; Belharouak, I.; Amine, K. High-Energy Cathode Material for Long-Life and Safe Lithium Batteries. *Nat. Mater.* **2009**, *8*, 320−324.

(167) Chen, S.; Zheng, J.; Mei, D.; Han, K. S.; Engelhard, M. H.; Zhao, W.; Xu, W.; Liu, J.; Zhang, J.-G. High-Voltage Lithium-Metal Batteries Enabled by Localized High-Concentration Electrolytes. *Adv. Mater.* **2018**, *30*, 1706102.

(168) Tatara, R.; Yu, Y.; Karayaylali, P.; Chan, A. K.; Zhang, Y.; Jung, R.; Maglia, F.; Giordano, L.; Shao-Horn, Y. Enhanced Cycling Performance of Ni-Rich Positive Electrodes (NMC) in Li-Ion Batteries by Reducing Electrolyte Free-Solvent Activity. *ACS Appl. Mater. Interfaces* **2019**, *11*, 34973−34988.

(169) Shyamsunder, A.; Beichel, W.; Klose, P.; Pang, Q.; Scherer, H.; Hoffmann, A.; Murphy, G. K.; Krossing, I.; Nazar, L. F. Inhibiting Polysulfide Shuttle in Lithium-Sulfur Batteries through Low-Ion-Pairing Salts and a Triflamide Solvent. *Angew. Chem., Int. Ed.* **2017**, *56*, 6192−6197.

(170) Feng, S.; Huang, M.; Lamb, J. R.; Zhang, W.; Tatara, R.; Zhang, Y.; Zhu, Y. G.; Perkinson, C. F.; Johnson, J. A.; Shao-Horn, Y. Molecular Design of Stable Sulfamide- and Sulfonamide-based Electrolytes for Aprotic Li-O$_2$ Batteries. *Chem.* **2019**, *5*, 2630−2641.

(171) Xue, W.; Shi, Z.; Huang, M.; Feng, S.; Wang, C.; Wang, F.; Lopez, J.; Qiao, B.; Xu, G.; Zhang, W.; et al. FSI-Inspired Solvent and "Full Fluorosulfonyl" Electrolyte for 4 V Class Lithium-Metal Batteries. *Energy Environ. Sci.* **2020**, *13*, 212−220.

(172) Xue, W.; Gao, R.; Shi, Z.; Xiao, X.; Zhang, W.; Zhang, Y.; Zhu, Y. G.; Waluyo, I.; Li, Y.; Hill, M. R.; et al. Stabilizing Electrode-Electrolyte Interfaces to Realize High-Voltage Li‖LiCoO$_2$ Batteries by a Sulfonamide-based Electrolyte. *Energy Environ. Sci.* **2021**, *14*, 6030−6040.